
LISA Frequency Control White Paper

Daniel Shaddock^{1,2}, Kirk McKenzie¹, Robert Spero¹, Jeffrey Livas³, Ira Thorpe³, Brent Ware¹, Glenn de Vine¹, Danielle Wuchenich^{1,2}, Kenji Numata³, Gerhard Heinzel⁴, Benjamin Sheard⁴, Juan José Esteban Delgado⁴, Felipe Guzmán⁴, Antonio Francisco Garcia Marin⁴, Peter Gath⁵, Hans-Reiner Schulte⁵, David Robertson⁶, Harry Ward⁶, Jordan Camp³, Guido Mueller⁷, Roger Diehl¹, Moshe Pniel¹, Robin Stebbins³, Mansoor Ahmed³, Stephen Merkwitz³, Vinzenz Wand⁷, Yinan Yu⁷, Dylan Sweeney⁷, Alix Preston⁷, Shawn Mitryk⁷, Oliver Jennrich⁸, Paul McNamara⁸, Marcello Sallusti⁸, Alberto Gianolio⁸, Luigi D'Arcio⁸, Karsten Danzmann⁴, Dennis Weise⁵, Pete Bender⁹, and Bill Klipstein¹

¹*Jet Propulsion Laboratory, California Institute of Technology*

²*The Australian National University*

³*NASA Goddard Space Flight Center*

⁴*Max Planck Institut für Gravitationsphysik (Albert Einstein Institut)*

⁵*Astrium*

⁶*University of Glasgow*

⁷*University of Florida*

⁸*European Space Agency*

⁹*JILA, University of Colorado, Boulder*

July 30, 2009

Contents

1	Introduction	4
I	Laser Frequency Control Subsystems	5
2	Pre-stabilization	5
2.1	Cavity Stabilization	5
2.2	Tunable Stabilized Lasers	8
2.3	Frequency Acquisition	11
2.4	Iodine Stabilization	11
2.5	Mach-Zehnder Stabilization	14
3	Arm Locking	26
3.1	Measurement Architecture for Arm Locking	26
3.2	Frequency Noise After Arm Locking	27
3.3	Modified Dual Arm Locking	28
3.4	Laser Frequency Pulling	30
3.5	Noise Limits	34
3.6	The Arm Locking Controller	37
3.7	Summary	41
4	Time-Delay Interferometry	43
4.1	Ranging Limited Performance	43
4.2	Ranging System	46
4.3	Algorithm Errors	51
4.4	Interpolation	52
4.5	Analog Chain	56
4.6	Phasemeter Digital Signal Processing	60
4.7	Scattered Light	61
4.8	Summary	64
II	Frequency Noise Suppression System Options	65
5	Fixed Cavity	66
5.1	Design Summary	66
5.2	Performance	67

6	Arm Locking Only	67
6.1	Design Summary	68
6.2	Performance	68
7	Arm Locking with Tunable Cavity Pre-stabilization	68
7.1	Design Summary	69
7.2	Performance	71
8	Arm Locking with Mach-Zehnder Pre-stabilization	71
8.1	Design Summary	71
8.2	Performance	74

1 Introduction

The LISA Frequency Control Study Team was established to provide a forum for practitioners to understand existing work in the field. The study team, formed in July 2008, participated in a series of teleconferences leading up to a meeting at Caltech from October 28-30, 2008. This white paper documents the state of knowledge in the area of laser frequency control for LISA.

Part I summarizes the performance of component subsystems for laser frequency noise control and suppression. Section 2 describes techniques for laser pre-stabilization to length references and atomic transitions. Section 3 presents a possible implementation of arm locking along with a detailed analysis of the predicted performance. Section 4 summarizes the noise suppression capabilities of Time-Delay Interferometry. Part II describes how individual frequency noise suppression techniques are combined into systems and estimates their levels of frequency stability. Four options are considered: fixed cavity; arm locking; cavity pre-stabilization and arm locking; and Mach-Zehnder pre-stabilization and arm locking.

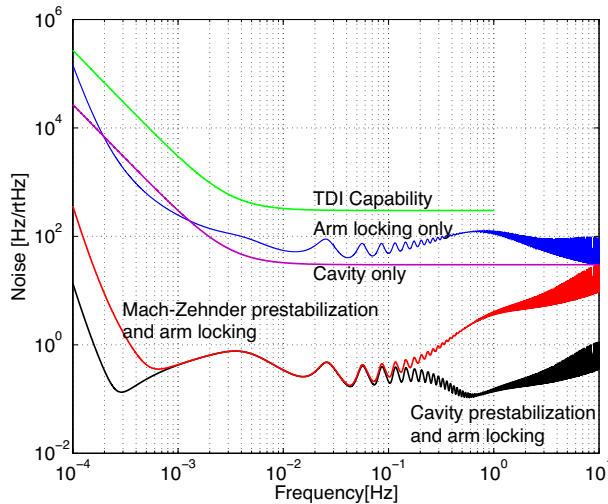


Figure 1: Comparison of predicted laser frequency noise for different stabilization system options. Arm length mismatch of $\Delta\tau = 0.026$ s. Also shown is the noise suppression capability of TDI, assuming 1 m ranging error.

The predicted frequency noise produced by these four options is shown in Figure 1. Also shown is the noise suppression capability of Time-Delay Interferometry (assuming 1 m arm length knowledge accuracy). This level represents the maximum allowable laser frequency noise consistent with the LISA error allocation.

Part I

Laser Frequency Control Subsystems

2 Pre-stabilization

Pre-stabilization is the term given to the first stage of frequency noise control that reduces the free-running noise of a laser by locking the laser to a reference. The reference can be either an absolute reference, such as an atomic or molecular system, or it can be a relative reference, such as an optical cavity. Only one pre-stabilization system is required at any time to stabilize the master laser. The other lasers will inherit the frequency stability of the master laser via phase-locking.

2.1 Cavity Stabilization

Optical cavities provide a relatively simple form of frequency stabilization that has been well studied in the laboratory. A cavity is formed from two or more low-loss mirrors arranged so that light may circulate between them [1]. A laser beam is coupled into the cavity via one of the mirrors. If the incident and circulating beams are in phase, light builds up in the cavity and it is said to be on resonance. Cavity-based laser stabilization works by diverting a small fraction of light from the laser to the cavity, detecting the resonant light, and controlling the laser frequency to maintain the resonance condition with high accuracy. The ultimate achievable frequency stability, $\Delta\nu$, is limited by the fractional length stability, $\Delta L/L$. By building the cavity with thermally stable materials, $\Delta L/L$ can be 10^{-13} or smaller, which would give $\Delta\nu = 30$ Hz.

It is important to note that the cavity does not provide an absolute frequency reference. Instead, there is a comb of transmission peaks spaced by the cavity's free spectral range, any one of which can provide the reference signal.

The standard technique used for stabilizing lasers to optical cavities for high precision applications is based on a method known as Pound-Drever-Hall (PDH) locking [2, 3]. By phase-modulating the incident beam and demodulating the reflected power at the same frequency, PDH generates a zero-crossing error signal centered around the cavity resonance. This error signal is then used by a control system to match the incident laser field to the cavity resonance. Using the reflected beam for the error signal avoids a time delay and therefore the resulting gain limitation that occurs when using a cavity with a very long storage time.

2.1.1 Key Parameters and Requirements

The cavity should have a moderately high finesse ($\sim 10,000$) to maximize the slope of the error signal while avoiding the technical issues associated with extremely high finesse

cavities. For the LISA application, the cavity should be designed to minimize thermally-induced changes in the optical path length, typically the dominant source of noise at sub-Hz Fourier frequencies. Laboratory cavities used in this regime are typically Fabry-Perot cavities consisting of low-loss mirrors that are contacted or otherwise bonded onto a rigid spacer of low-expansion material such as Zerodur or ULE. The cavity is then placed in a vacuum chamber and isolated from environmental disturbances such as temperature fluctuations and vibration. Table 1 shows some of the typical parameters for a Fabry-Perot style cavity. High finesse cavities require careful spatial alignment and mode matching for optimum performance.

Table 1: Typical Fabry-Perot Reference Cavity Parameters

Parameter	Value	Comments
<i>Cavity Parameters</i>		
Free Spectral Range (FSR)	~ 500 MHz	~ 30 cm length cavity spacer
Finesse	$\sim 10,000$	Large error signal slope
Cavity Linewidth (FWHM)	~ 50 kHz	FSR/Finesse
Power into cavity	~ 1 mW	Performance limited by thermal fluctuations, not shot noise
<i>PDH Parameters</i>		
Modulation Frequency	> 5 MHz	Above the band of technical laser noise
Loop Bandwidth	~ 10 kHz - 30 kHz	Limited by piezo-electric laser frequency actuator

2.1.2 Basic System Configuration

Figure 2 shows the basic configuration of a PDH frequency stabilization system with the components listed in detail in Table 2.

2.1.3 Reference Performance

The frequency stability requirement from the LISA pre-Phase A report [5] is a residual frequency noise spectral density in the LISA measurement band of:

$$\nu(f) = 30 \text{ Hz}/\sqrt{\text{Hz}} \cdot \sqrt{1 + (3 \text{ mHz}/f)^4}. \quad (1)$$

This performance level has been achieved in several laboratories, for example, [6].

Table 2: List of the most commonly used components for the standard Pound-Hall-Drever frequency stabilization to a fixed cavity reference scheme.

Device	Type	Function	Comments
Laser	Optical	Light source to be stabilized	Must have sufficient frequency tuning bandwidth (~ 100 kHz) to suppress free-running noise.
Phase modulator	Electro-Optical	Modulates optical phase of beam according to electric drive amplitude	Typically an electro-optic modulator (EOM). Bulk-crystal versions must be made resonant to reduce drive voltage. Waveguide versions have naturally low drive voltage.
Polarizing Beam Splitter (PBS)	Optical	Separates incoming from outgoing beams	Unnecessary in a ring cavity
Quarter wave plate (QWP)	Optical	Separates incoming from outgoing beams	Unnecessary in a ring cavity
Local Oscillator (LO)	Electronic	Sinusoidal signal source. Drives modulator and demodulator	Could be analog or digital (NCO)
Demodulator	Electronic	Demodulates light to generate error signal	Could be analog (mixer) or digital (multiplier)
Filter	Electronic	Shapes error signal to generate laser control signal	Could be analog or digital
Photoreceiver (PR)	Electronic	Detects reflected power from the cavity	

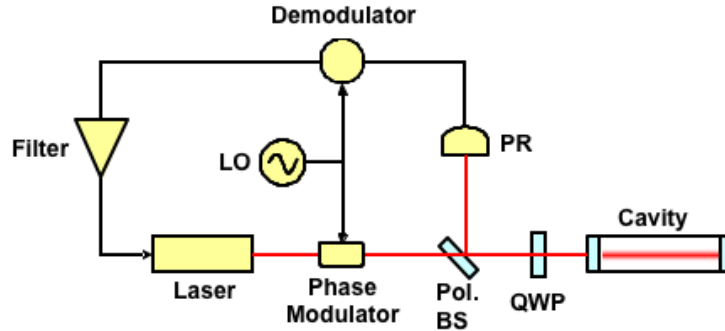


Figure 2: Block diagram of a standard Pound-Drever-Hall laser stabilization system showing a reference cavity, phase modulator, polarizing beam splitter (Pol. BS), quarter-wave plate (QWP), and photoreceiver (PR). The local oscillator (LO) is the sinusoidal signal source driving the modulator and demodulator.

2.2 Tunable Stabilized Lasers

The ability to tune the central frequency of a pre-stabilized reference without substantially compromising the frequency noise performance is important for combining and/or cascading the pre-stabilization with other frequency references such as the arms of the LISA constellation. In this section we consider modifications to the basic cavity locking techniques that allow the central frequency to be tuned. Other methods for achieving tunability, such as acousto-optic modulators and offset-locked lasers, are possible but are not discussed here.

2.2.1 Tunability Requirements

A frequency tuning range of more than a free spectral range of the reference cavity, typically several hundred MHz (see Table 1), would provide the greatest flexibility. In Section 3 we show that arm locking could pull the laser frequency by up to 300 MHz from its nominal value due to errors in the Doppler estimate. However, this Doppler estimate is obtained assuming no pre-stabilization. With $30 \text{ Hz}/\sqrt{\text{Hz}}$ pre-stabilization and 200 s for Doppler estimation, the expected frequency pulling is less than 10 MHz. In addition, the frequency response of the tunability should be sufficient to support a high gain auxiliary locking scheme such as arm locking. Furthermore, the tuning capability must not substantially degrade the pre-stabilized noise performance within the LISA measurement band.

2.2.2 PZT Tunable Cavities

One way to make a frequency reference tunable is to include an actuator that can change the optical path length inside the resonant cavity. This can be accomplished by changing the cavity length. Figure 3 shows an example design for a Fabry-Perot cavity with a piezoelectric element in the cavity. The PZT has a silver coating on the wide faces that allow hydroxide bonding to be used in joining the fused silica mirror and the Zerodur spacer. The PZT has a silver coating on the wide faces that allow hydroxide bonding to be used in joining the fused silica mirror and the Zerodur spacer.

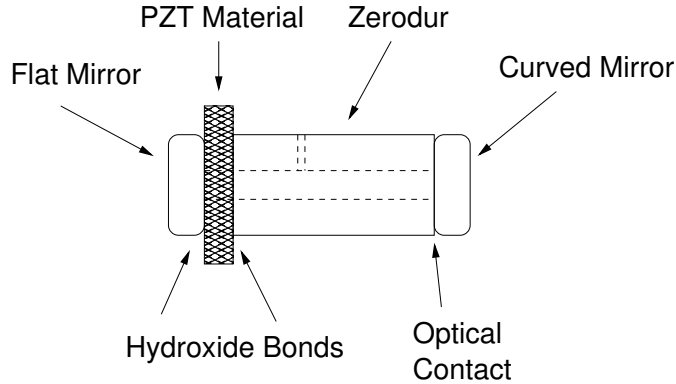


Figure 3: Side view of the PZT cavity.

The best measurements achieved so far with this technique show excess noise ($\sim 2 \text{ kHz}/\sqrt{\text{Hz}}$).

2.2.3 Electro-optic Modulator Tuning

Another method for tuning a laser pre-stabilized to a fixed frequency reference is through the use of sideband locking [7]. In sideband locking, an additional tone is added to the phase modulator drive that generates the PDH error signal. This tone, a sideband to the laser carrier, is locked to the reference cavity and as the frequency of the tone is varied, the center frequency of the pre-stabilized laser is tuned. The required components are identical to those shown in the block diagram in Figure 2, except that the modulator must be broadband, not resonant, to allow for tunability, and the electronic signal driving the modulator must be a slightly more complex waveform than the sinusoidal reference required for standard PDH locking. No modifications to the reference cavity are required, and standard PDH is recovered by removing the sideband tone. This technique is described in detail in Reference [7]. Similar performance as compared to a standard PDH system has been demonstrated (Figure 4), however not at the level of $30 \text{ Hz}/\sqrt{\text{Hz}}$.

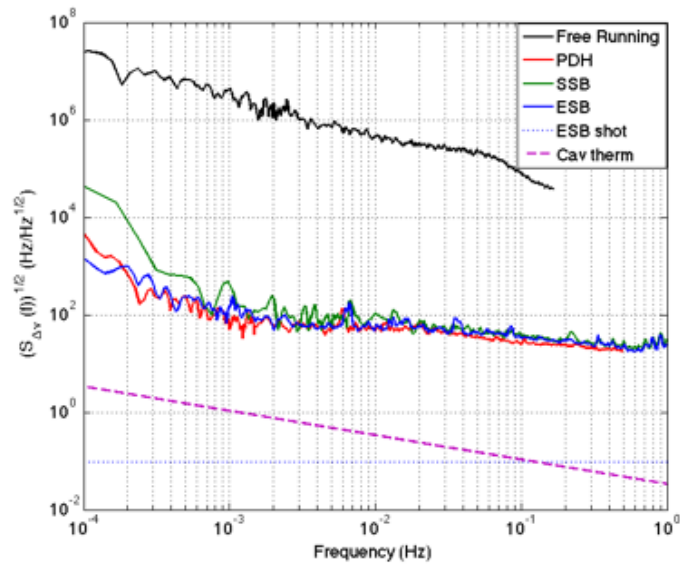


Figure 4: Measured frequency noise of a sideband-locked pre-stabilized laser [7].

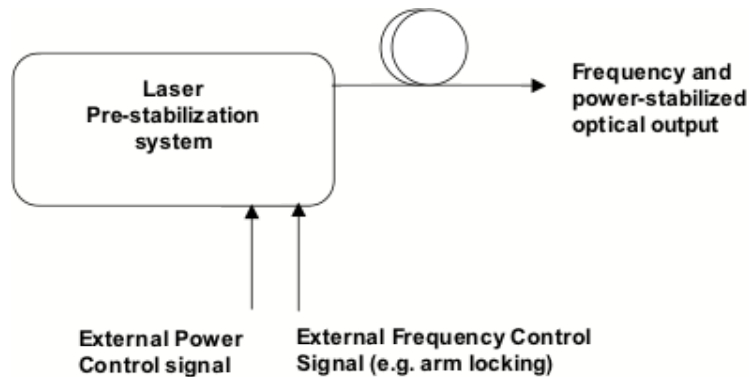


Figure 5: Simplified interface drawing showing key interactions with other systems needed for frequency stabilization. Not shown are standard interfaces to the spacecraft bus for electrical power, housekeeping information, and normal command and control.

2.3 Frequency Acquisition

The process of setting a given laser to a specified frequency offset from the incoming laser frequency is known as “frequency acquisition” and is necessary to make the science measurements. The relative offsets of each laser in the LISA system are pre-computed and uploaded to each spacecraft as part of the frequency plan. The use of an absolute frequency reference makes it possible in principle to use a deterministic procedure to set the individual lasers to specific offset frequencies. If all lasers are first locked to this reference, they can be offset locked by the specified amount simply by tuning. Alternatively, an absolute reference can be used as a diagnostic device to measure the frequency of a laser locked to a relative reference and to decide how to tune the offsets to the correct value.

Without an absolute frequency reference, it is necessary to search for the correct frequency offset by changing the operating state of one in a pair of heterodyning lasers. Although the absolute frequency is not known as precisely as it could be when determined with an absolute reference, it is known approximately from the characterization of the lasers during ground testing. For example, the lasing frequency of a non-planar ring oscillator (NPRO) is a function of the pumping conditions (the current to the pump diode) and the temperature of the crystal. The frequency of the laser can be measured as a function of these parameters and then the parameters may be used to set the correct operating point of the laser frequency. The parameters may be swept while monitoring for a beat note. Preliminary tests [8] of a scanning procedure have shown beat note acquisition of lasers up to 5 GHz apart is possible in less than 1 minute using the 20 MHz bandwidth analog chain and phasemeter. Although these tests did not use representative LISA power levels, the algorithm was designed to work with the anticipated LISA signal-to-noise ratio.

2.4 Iodine Stabilization

Laser frequency stabilization employing iodine has many similarities to cavity stabilization [9]. Instead of stabilizing the frequency to the resonance of an optical cavity, the laser frequency is referenced to a hyperfine transition of molecular iodine, I_2 . An additional complexity over cavity stabilization is the need to frequency-double a small portion of power from the fundamental laser frequency, changing the wavelength from 1064 nm to 532 nm in order to access the strong, narrow hyperfine transitions of iodine. The frequency of the transition is determined by the molecular physics of the iodine system; this transition frequency provides an absolute frequency reference. Known molecular transitions at 1064 nm are many orders-of-magnitude weaker than iodine at 532 nm and would require more complex arrangements to obtain the required frequency stability.

Like an optical cavity, the iodine transition has both an amplitude and phase response. A number of different methods can be employed to extract an error signal from the absolute frequency of the hyperfine transition. A laser can be locked on resonance with the transition in a similar feedback scheme to the PDH technique [10, 11]. The narrow hyperfine transition

is accessed by using two counter-propagating beams to limit Doppler effects, while the broad absorption features are accessed by a single transmitted beam.

Frequency stabilization with iodine could offer a number of features for LISA, including:

- An absolute frequency reference for reducing risk in frequency lock acquisition. To ensure that the lasers on separate spacecraft have frequencies within 20 MHz (so that their beat notes will appear on the photodiode), it will be necessary to use a frequency-scanning algorithm that will be implemented in parallel with a spatial acquisition algorithm. There is no wavefront sensing available until the beat note is < 20 MHz. The use of iodine would fix the laser frequencies to an absolute value, so that their absolute frequencies are within a few kHz;
- The iodine system is less sensitive to environmental disturbances than a cavity, thus its use may simplify aspects of the payload systems engineering. Iodine would not require any external temperature stabilization (for employment as a wavemeter only), potentially eliminating the need for the additional mass associated with thermal isolation. Its requirement for alignment control is also reduced by approximately a factor of 10 compared to a cavity;
- Many of the iodine components have been flight qualified: including gas cells, doubling crystal, modulator, and optics.

A number of options exist for the iodine implementation, of varying degrees of complexity. They range from full pre-stabilization of the laser, including feedback control, to a simple wavemeter which only reads out the absolute laser frequency. All options have the following characteristics:

- A high efficiency doubling waveguide, providing several mW of green (532 nm) light with ~ 100 mW IR (1064 nm) light input. The waveguide is operated at room temperature, eliminating the need for a heater;
- A fully fiber-coupled implementation, including waveguide, gas cell, and modulators.

Below we describe in more detail the options for the iodine implementation, including schematic layouts and noise performance.

1. Pre-stabilization: this configuration will allow for pre-stabilization of the in-band laser frequency, as well as fix the absolute frequency. It requires the use of modulators and a cooler. Two sub-options are given, along with measured noise of each option.
 - (a) Complete setup (Figure 6):
 - i. $50 \text{ Hz}/\sqrt{\text{Hz}}$ at 1 mHz;
 - ii. $\sim \text{kHz}$ absolute accuracy.

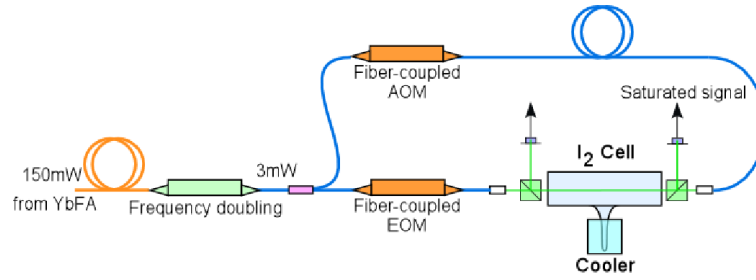


Figure 6: Complete iodine frequency stabilization setup.

- (b) Simplified setup (Figure 7):
- i. $200 \text{ Hz}/\sqrt{\text{Hz}}$ at 1 mHz;
 - ii. $\sim 10 \text{ kHz}$ absolute accuracy.

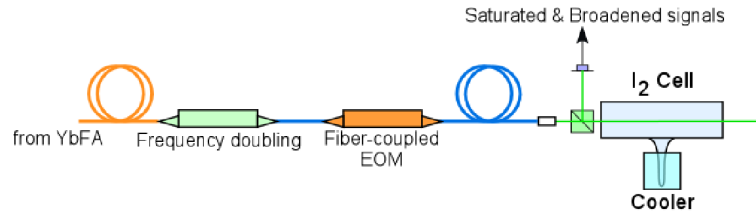


Figure 7: Simplified iodine frequency stabilization setup.

2. Wavemeter: this option provides solely for the absolute frequency reference. It is a very simplified setup, using no modulators, heater, cooler, or feedback electronics.

- (a) Fine wavemeter configuration (Figure 8):
- i. Mechanical modulation on mirror;
 - ii. On hyperfine resonance: $\sim 10 \text{ kHz}$;
 - iii. Coarse knowledge: $\sim 10 \text{ MHz}$.

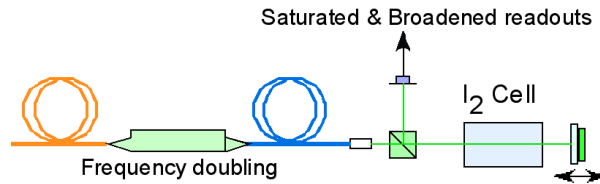


Figure 8: Fine wavemeter configuration.

- (b) Coarse wavemeter configuration (Figure 9):

- i. Coarse knowledge: ~ 10 MHz.

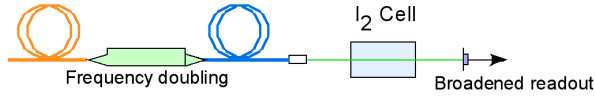


Figure 9: Course wavemeter configuration.

2.4.1 Performance Improvement Options

Additional research on the iodine system will involve looking into further simplifications. For example, it may be possible to simultaneously shorten the iodine cell to several centimeters in length while raising the iodine gas density by eliminating the cooler. This could result in a simpler and more compact system, though the noise and stability of this possibility remains to be quantified.

2.4.2 Comparison of Absolute References at 532 nm and 1064 nm

A comparison of possible absolute optical frequency references at 532 nm and 1064 nm is shown in Table 3. Although there are other alternatives, it appears that Doppler-free operation of molecular iodine offers the best performance.

2.5 Mach-Zehnder Stabilization

The LISA Technology Package (LTP) on board LISA Pathfinder uses an unequal path length, heterodyne Mach-Zehnder interferometer to measure and actively stabilize the laser frequency fluctuations [12, 13]. In this approach the path length mismatch of the interferometer is used as the frequency reference. In comparison to an optical cavity or molecular reference, the technique has a wide operating range and does not require a complex lock acquisition procedure. Frequency tuning can be provided by purely electronic means and does not require physically changing the path length (or resonance frequency) of the frequency reference.

2.5.1 System Description

Figure 10 shows the basic system layout for a heterodyne Mach-Zehnder interferometer with a path length mismatch that could be integrated on the LISA optical bench. The reference interferometer measures the phase difference (ϕ_R) between the lasers on adjacent optical benches within one LISA satellite. This reference interferometer already exists in the current LISA optical bench design. An additional interferometer with unequal path lengths could be placed on the optical bench to measure the frequency noise of the master laser, as will be implemented in LISA Pathfinder [12, 13].

Table 3: Comparison of Absolute Frequency References

System	Linewidth	Pros	Cons & Special Issues
Iodine (I_2) @ 532 nm, Doppler-free	~ 1 MHz	Long History Well-identified lines High Stability demo-ed	Doubling Crystal Needed (30-50° C) Cell cooling preferable ($\sim 5^\circ$ C) Repeatability: >few kHz
Iodine (I_2) @ 532 nm, Doppler-Broadened	~ 700 MHz	Simple Setup Very Strong lines	(Heated) Doubling Crystal Needed (30-50° C) Cell cooling may be needed $10^3 \times$ worse stability than Doppler-free Repeatability: > few MHz
Cesium (Cs_2)	~ 10 MHz	Well-known RF reference Flight heritage in GPS No doubling crystal	Weakness of line, large temperature shift Heater ($\sim 200^\circ$ C) needed Cavity may be needed
Acetylene C_2H_2 or C_2HD , Doppler-free	~ 1 MHz	Well-known $1.5 \mu m$ reference No doubling crystal No heater	Weakness of line Cavity may be needed
Carbon dioxide (CO_2)	~ 2 GHz	No Doubling Crystal	Weakness of line Small number of demonstrations

The main difference between this system and that of LTP is that the beat note is generated by interference with an offset phase-locked laser at a variable frequency difference of 2 to 20 MHz rather than interference between two beams produced by acousto-optic modulators at a constant frequency difference of 1 to 2 kHz.

The output of this additional interferometer (ϕ_F) could be used to measure frequency fluctuations of the laser and to actively stabilize the master laser frequency. Thus the proposed configuration contains two control loops:

- (ϕ_R – frequency offset) Locks the slave laser to the master laser as in the LISA baseline;

- $(\phi_F - \phi_R - \text{tuning bias})$ Locks the master laser frequency to the length difference.

The laser on the other bench (the slave laser) is offset phase-locked to the master with high gain/bandwidth with a constant frequency offset:

$$\nu_s = \nu_M + f_{\text{het}}, \quad (2)$$

with $2 \text{ MHz} \leq f_{\text{het}} \leq 20 \text{ MHz}$. This phase-locking arrangement will be used in any case.

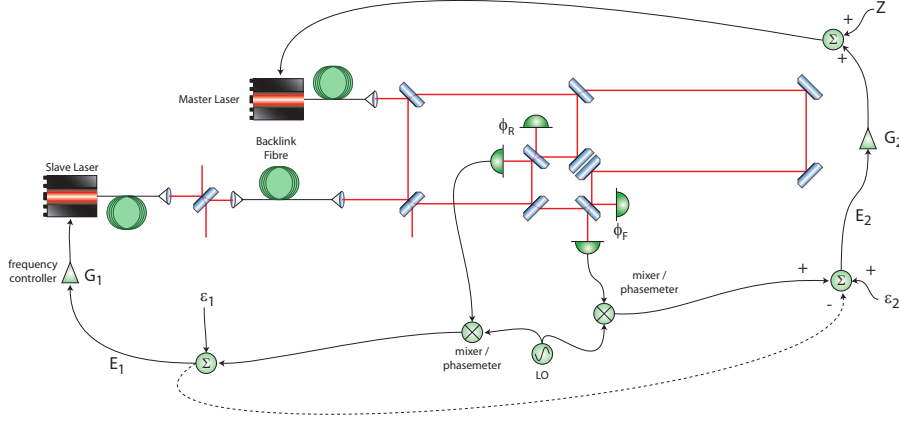


Figure 10: Basic system schematic. The interferometer with the ϕ_R readout is in the current LISA optical bench design. The ϕ_F interferometer is the proposed additional interferometer for measuring and actively suppressing the laser frequency noise, as in LISA Pathfinder.

After phase-locking, the closed loop phase noise of the slave laser is given (in the frequency domain¹) by

$$P_{s|\text{cl}} = \frac{G_1}{1 + G_1} P_M - \frac{G_1}{1 + G_1} \epsilon_1 + \frac{1}{1 + G_1} P_{s|\text{fr}}, \quad (3)$$

where

- $P_{s|\text{fr}}$ - free-running slave laser phase noise;
- $P_{s|\text{cl}}$ - closed loop slave laser phase noise;
- P_M - master laser phase noise;
- ϵ_1 - error point noise (sensor noise) for loop 1;

¹Note that so far no assumptions have been made about the properties of the signals (e.g. correlations) and so the quantities should be considered as Fourier transforms with phase information and not spectral densities, which would be added in quadrature for uncorrelated noise sources.

- G_1 - controller transfer function for loop 1 (e.g. P, PI controller, integrator “built-in” from frequency to phase conversion).

Equation 3 shows that in the high gain limit:

- The free-running slave phase noise is suppressed;
- The performance is limited by sensor noise ϵ_1 ;
- The slave laser tracks the master laser phase noise with accuracy $\frac{G_1}{1+G_1} \approx 1$.

Offset phase-locking the slave laser fixes the beat note frequency for both the ϕ_R and ϕ_F interferometers to the chosen frequency offset, but does not have any effect on the frequency of the master laser. The master laser can be freely tuned, while the slave laser tracks these changes. Thus, the first loop only controls the frequency difference between the two lasers.

2.5.2 Master Laser Frequency Control Loop

Measuring the phase of the beat note for the ϕ_F interferometer produces the following error signal for the second control loop (used to stabilize the master laser frequency):

$$E_2 = \epsilon_2 - P_M e^{-j\omega\tau} + P_{s|cl}. \quad (4)$$

This assumes that the propagation delay from the slave laser to ϕ_F is identical to the delay to ϕ_R . The master laser has an additional propagation delay of $\tau = \Delta L/c$ for ϕ_F compared to ϕ_R .

Introducing an offset ϵ_2 to the error point of the master laser control loop can be used to tune the master laser frequency (which the slave laser tracks due to the offset phase-lock).

Substituting the closed loop slave laser noise given in Equation 3 into Equation 4 gives:

$$E_2 = \epsilon_2 + \left[\frac{G_1}{1+G_1} - e^{-j\omega\tau} \right] P_M - \frac{G_1}{1+G_1} \epsilon_1 + \frac{1}{1+G_1} P_{s|fr}. \quad (5)$$

Therefore the approach of using only the phase measurement for the ϕ_F interferometer leads to a transfer function for master laser phase noise that depends on the slave laser controller design, significantly complicating the controller design for the master laser control loop. However, the technique can be modified as described in the next subsection to simplify the response to the master laser frequency and make the design independent of the slave laser control loop.

2.5.3 Subtraction of Residual Phase-Lock Error

The closed loop error point for the slave laser is given by:

$$E_1 = \frac{P_{s|fr}}{1+G_1} + \frac{G_1}{1+G_1} P_M - P_M + \epsilon_1 - \frac{G_1}{1+G_1} \epsilon_1. \quad (6)$$

Subtracting this from the error point for the second control loop leads to:

$$E_2 - E_1 = \left(\frac{G_1}{1+G_1} - e^{-j\omega\tau} + 1 - \frac{G_1}{1+G_1} \right) P_M \\ - \frac{1}{1+G_1} P_{s|fr} + \frac{P_{s|fr}}{1+G_1} - \frac{G_1}{1+G_1} \epsilon_1 + \frac{G_1}{1+G_1} \epsilon_1 \\ + \epsilon_2 - \epsilon_1 \quad (7)$$

$$, = [1 - e^{-j\omega\tau}] P_M + \epsilon_2 - \epsilon_1, \quad (8)$$

which is independent of G_1 and P_s . This approach allows the design of the second (master laser) control loop to be independent of the first (slave laser) control loop. Although this suggests that if the subtraction has perfect fidelity the slave laser need not be locked to the master, the slave laser still needs to be phase-locked in order to keep the beat note frequency within the photodiode/phasemeter bandwidth.

For frequencies below the inverse delay time τ^{-1} , the transducer gain of the mismatched path length interferometer is:

$$\frac{\delta\Phi_F}{\delta\nu_M} \approx \frac{2\pi\Delta L}{c}, \quad (9)$$

thus providing an error signal which can be used to control the frequency of the master laser.

2.5.4 Master Laser Closed Loop Noise

Defining:

$$L_2 = G_2 [1 - e^{-j\omega\tau}], \quad (10)$$

the closed-loop master laser noise is then given by:

$$P_{M|cl} = \frac{P_{M|fr}}{1+L_2} - \frac{G_2}{1+L_2} \epsilon_1 - \frac{G_2}{1+L_2} \epsilon_2. \quad (11)$$

The effect of offsets in the error point of the phase of the master laser is given by:

$$\frac{\partial P_{M|cl}}{\partial \epsilon_2} = \frac{G_2}{1+L_2} \approx \frac{1}{j\omega\tau}, \quad (12)$$

where the approximation is valid for large gain and frequencies low compared to the inverse delay time. In terms of the master laser frequency this corresponds to:

$$\frac{\partial \nu_{M|cl}}{\partial \epsilon_2} \approx \frac{1}{2\pi\tau}, \quad (13)$$

which is the frequency tuning response at low frequencies for high loop gain.

2.5.5 Controller Transfer Functions (Preliminary Design)

A slave laser phase-lock bandwidth of 20 kHz is assumed. Figure 11 shows preliminary controller designs for the two controllers shown in Figure 10. The corresponding Nyquist diagrams are shown in Figure 12.

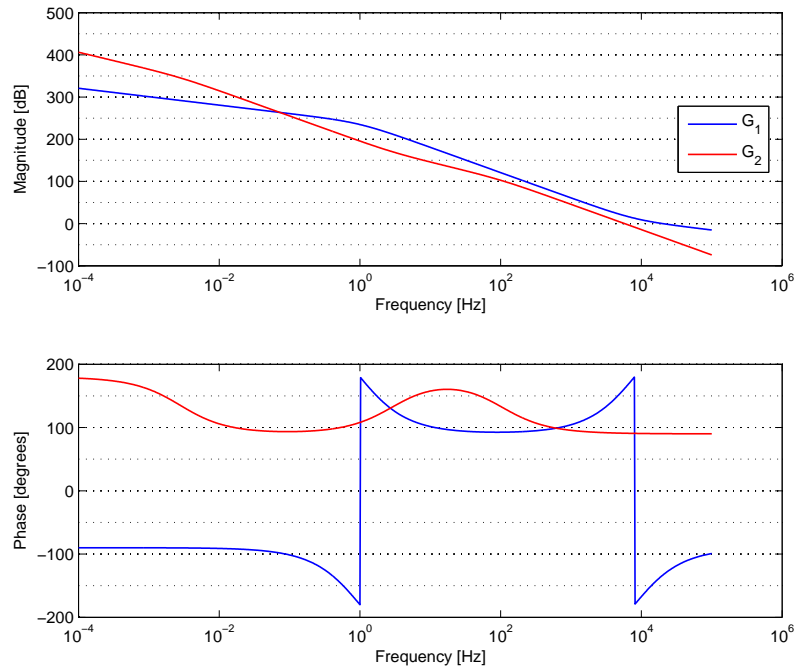


Figure 11: Preliminary controller designs. Note that the controller transfer functions shown include a pole at DC due to frequency-to-phase conversion (i.e. the laser actuators act on frequency and not phase directly).

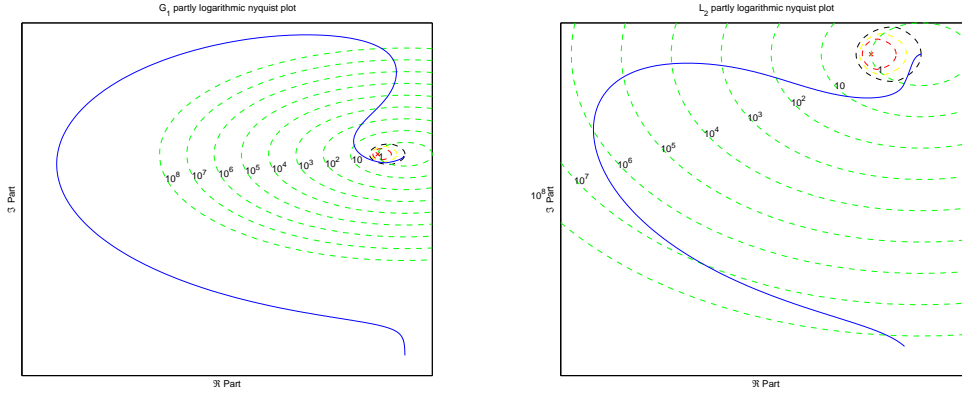


Figure 12: Partly logarithmic Nyquist plot for the slave (left) and master (right) laser control loops.

2.5.6 Interfaces with Other Subsystems

Phase Measurement Subsystem Interfaces

- Assuming that the two lasers are phase-locked with a fixed frequency offset using the ϕ_R interferometer output as the error signal, there are two ways to generate the offset locking error signal: use the tracking phasemeter's phase output and numerically subtract a ramp of the desired slope; or implement a separate multiplier (mixer) which is not tracking but instead driven by a sine wave of the desired frequency.
- The phasemeter's performance above 1 Hz is also important and will influence the optimal unity gain frequency of the feedback.
- Any corrections required to reach $1 \text{ pm}/\sqrt{\text{Hz}}$ performance (e.g. ADC jitter correction) may need to be implemented in real-time on the fast phasemeter outputs, unless it is common to both phase measurements (e.g. clock noise).

Laser Frequency Actuator Interfaces

The same laser actuator interface as for standard offset phase-locking is required. The split actuation due to limiting the bandwidth of the master laser control loop in order not to significantly increase the noise level at high frequencies is applied externally to the laser subsystem. Therefore no change to the laser frequency actuator interface is expected to be necessary.

Frequency Tunability for Arm Locking

Figure 13 shows the frequency tuning response for injecting offsets into the master laser frequency control loop (blue curve). Notice that for this input the bandwidth is restricted by the low loop bandwidth used in order to reduce the degradation of the laser noise above 10 Hz. The green curve shows the frequency tuning response for the input labeled Z in Figure 10, scaled by a factor of $1/(2\pi\tau)$ in order to compensate for the gain of the interferometer. The sum is shown as the red curve. Injecting the same signal into the offset and directly to the laser (compensating for the interferometer gain) provides a high bandwidth frequency actuation for implementing arm locking. The achievable tuning bandwidth in this approach is limited by the laser frequency actuators. This split actuation approach may also be useful for other types of tunable frequency references. Further investigation of the split actuation scheme for frequency tuning, in particular an experimental demonstration, is needed.

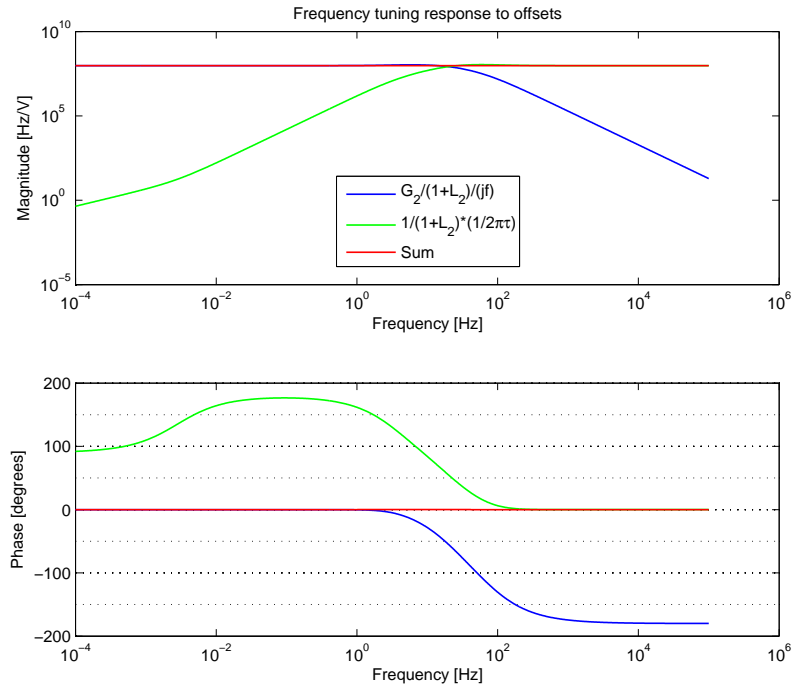


Figure 13: Frequency tuning response.

2.5.7 System Performance and Limitations

Like an optical cavity, the ultimate performance of this system is limited by stability of the reference:

$$\frac{\widetilde{\delta\nu}(f)}{\nu} = \frac{\widetilde{\delta x}(f)}{\Delta L}, \quad (14)$$

where $\widetilde{\delta x}(f)$ represents the path length fluctuations of the interferometer. However, additional noise introduced by associated readout electronics (photodetectors and phasemeters) can also limit performance.

Figure 14 shows the predicted system performance assuming a 50 cm path length mismatch and typical free-running laser frequency noise ($10 \text{ kHz}/\sqrt{\text{Hz}}$ at 1 Hz with $1/f$ noise shape). The assumed combined phasemeter and path length noise is

$$\epsilon_i = \frac{2\pi}{\lambda} \times 1 \text{ pm}/\sqrt{\text{Hz}} \times \sqrt{1 + \left(\frac{2.8 \text{ mHz}}{f \text{ Hz}}\right)^4}. \quad (15)$$

The phasemeter/path length noise of the two channels is assumed to be uncorrelated.

Notice that the closed loop frequency noise level intersects the free-running noise level at approximately 10 Hz for typical Nd:YAG NPRO lasers. For closed loop bandwidths above this frequency, the closed loop noise level would be higher than the free-running laser noise (which has a potential impact on the performance of other subsystems, e.g. the phasemeter). Therefore in the proposed design the bandwidth of the second loop is restricted to approximately 20 Hz.

In this simple model the closed loop frequency is limited primarily by the phasemeter noise of the two phasemeter channels used and results in a closed loop frequency noise level for the master laser of approximately $800 \text{ Hz}/\sqrt{\text{Hz}}$ in the 10 mHz to 1 Hz range.

2.5.8 Reference (LTP Engineering Model) Performance

Figure 15 shows the laser frequency stability achieved with a free-running standard NPRO stabilized to the frequency interferometer of the LTP optical bench engineering model measured by beating with an iodine-stabilized NPRO. The observed frequency stability matches the noise projection in the LTP band.

Figure 16 shows the closed loop frequency noise stability achieved with the LTP optical bench engineering model at the AEI Hannover. The red curve shows a comparison between an iodine-stabilized laser and a NPRO laser stabilized using the LTP optical bench engineering model. The red curve is therefore an “out-of-loop” measurement of the laser frequency stability. Note that in this case the system is gain limited (due to the low heterodyne frequency) and not sensor noise limited and that the closed loop noise is dominated by residual frequency fluctuations and not phasemeter noise or path length fluctuations. The orange curve shows a projection of the measured displacement noise (including the dummy

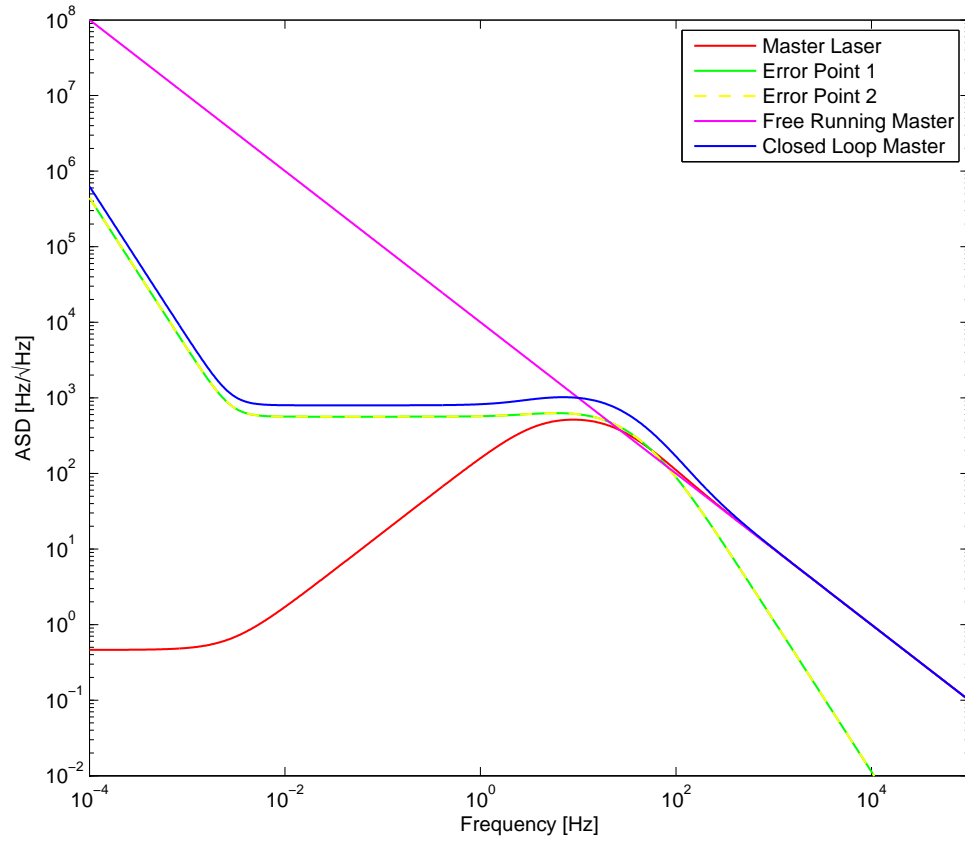


Figure 14: Closed loop frequency noise (blue trace) assuming a 50 cm path length mismatch for Mach-Zehnder pre-stabilization.

test masses which are mounted on metallic mounts), assuming a path length mismatch of 38 cm following the relationship:

$$\widetilde{\delta\nu}(f) = \frac{c}{2\pi\Delta L} \widetilde{\Phi}_{F-R}(f). \quad (16)$$

The orange curve is indicative of the performance that could be achieved if the loop gain was increased. The current loop gain is sufficient to reach the LTP requirement.

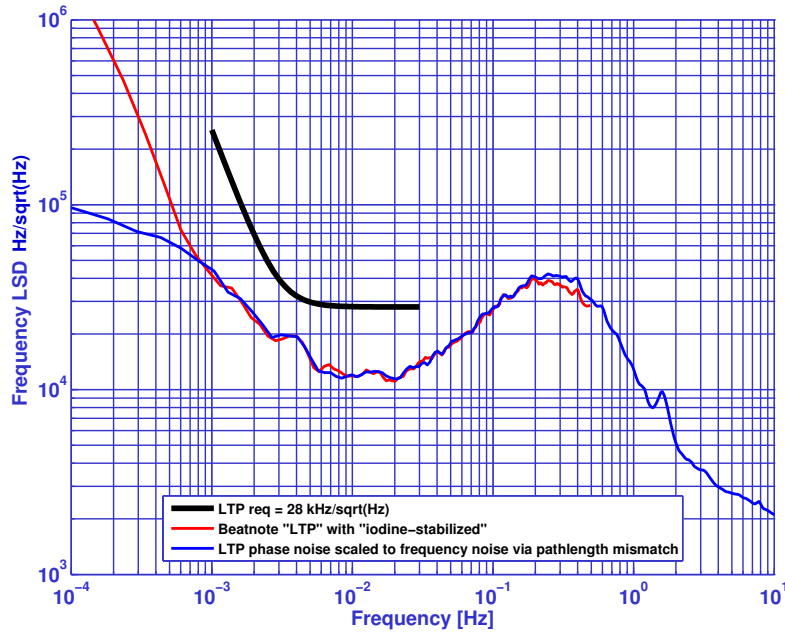


Figure 15: Laser frequency stability of the LTP optical bench engineering model measured with an iodine-stabilized NPRO reference and the projected performance.

2.5.9 Performance Improvement Options

The performance projection of Figure 16 (orange curve) was obtained using the LTP optical bench engineering model and LTP phasemeter (with a heterodyne frequency of approximately 1.6 kHz, which limits the achievable loop gain). The optical path included the dummy test masses using metallic mounts.

For a given path length/phasemeter performance the sensor noise and thus closed loop performance level of the technique can be improved by increasing the path length mismatch of the Mach-Zehnder. The path length mismatch used in this analysis (50 cm) could potentially be increased.

It may be possible to use a fixed heterodyne frequency which may allow optimization of the phasemeter performance for this heterodyne frequency.

2.5.10 Summary

The proposed LTP-style unequal arm length Mach-Zehnder frequency stabilization has the following requirements and characteristics:

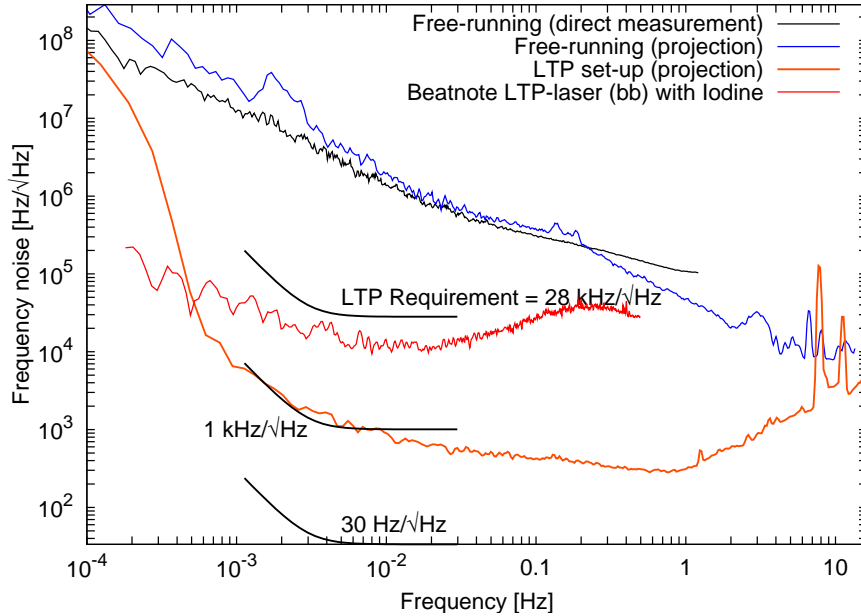


Figure 16: Measured LTP performance and projected sensor noise floor. The system meets the LTP requirement, however the system is not sensor noise limited. The performance could be significantly improved by increasing the loop gain. The orange curve is an estimate of the sensor noise floor.

- Several extra components (of the type that will be implemented in any case: mirrors, beam-splitters, photodiodes and phasemeter channels) are needed to implement an additional interferometer;
- Subtracting the reference phasemeter output from the frequency interferometer phasemeter output makes the master laser controller design independent of the phase-lock bandwidth of the slave laser;
- Extrapolation of phasemeter performance to frequencies above 1 Hz leads to worse than free-running laser frequency (above approx. 10 Hz for typical NPRO frequency noise) performance limit if a large bandwidth is used to stabilize the master laser. Therefore limiting the bandwidth is desirable;
- The target laser frequency can be tuned by subtracting a phase offset from the error signal before feeding it to the servo. A split feedback arrangement, where the (appropriately scaled) signal for frequency tuning is fed directly into the laser frequency input, appears to be feasible to overcome the bandwidth restriction that is desirable

due to the *assumed* high frequency phasemeter performance;

- Although the predicted performance may not be as good as that of a rigid cavity, the technique has some significant advantages. For example, the error signal is immediately available for any operating point (no lock acquisition procedure needed), and minimal additional hardware is required compared to other tunable frequency references.

3 Arm Locking

Arm locking is the second stabilization technique in the LISA frequency noise plan. Arm locking has developed significantly since the initial arm locking proposal by Sheard *et. al* [14]. Much of the risk associated with the unusual control system has been retired by hardware demonstrations [15, 16, 17, 18], simulations [19] and theoretical investigations [20]. Dual arm locking [21], the current baseline for in the LISA design, builds on the proposal of Enhanced arm locking [22]. This scheme uses combinations of phase measurements from two arms to increase the frequency of the first null of the sensor from $1/\tau \approx 30$ mHz to $1/(2\Delta\tau) > 2$ Hz, where $\Delta\tau$ is the 1/2 the difference in light travel round trip times of the two arms used (we define the average round trip time as $\bar{\tau}$). Moving the first null to outside the LISA band allows a more aggressive controller design below 2 Hz and eliminates, from the LISA science band, noise amplification due to the nulls.

Recent studies undertaken by members of the FCST have since extended the understanding of how arm locking would operate in LISA, the expected performance, and the issues that need to be addressed. This chapter gives an overview and reports issues associated with laser frequency pulling due to Doppler frequency error, noise limits, and the expected performance in LISA. Although the single and dual arm locking configurations are introduced, the performance is calculated using a modified dual arm locking, a hybrid of common and dual arm locking sensors, which delivers the frequency pulling characteristics and low-frequency noise coupling of common arm locking, but retains the control system advantages of dual arm locking.

3.1 Measurement Architecture for Arm Locking

Time-Delay Interferometry will be implemented in post processing by forming linear combinations of five low bandwidth (~ 3 Hz) phase measurements on each optical bench (with two optical benches per spacecraft) [23] with delays determined by inter-spacecraft ranging. These phase measurements are (1) inter-spacecraft measurement, (2) the backlink measurement, (3) the proof mass to optical bench measurement, (4) and (5), the beatnotes of the upper-upper and lower-lower clock sidebands. To form the displacement measurement, TDI will use the strap-down architecture [24], which combines the inter-spacecraft measurements, the proof mass to optical bench, and the backlink measurement to remove

spacecraft motion. Clock noise in the measurement can be removed using the beatnote of clock sidebands [25, 26, 27, 28, 29].

Unlike TDI, arm locking requires high bandwidth signals ($\sim 20\text{kHz}$), in real time, and has significantly less stringent noise requirements than the LISA science measurement. Given the relaxed noise requirements, we assume that arm locking will operate with the most simple measurement architecture - *using only the inter-spacecraft phase measurements*. An outcome of this simple measurement architecture is both clock noise and spacecraft motion will be present in the phase measurements used for arm locking.

3.2 Frequency Noise After Arm Locking

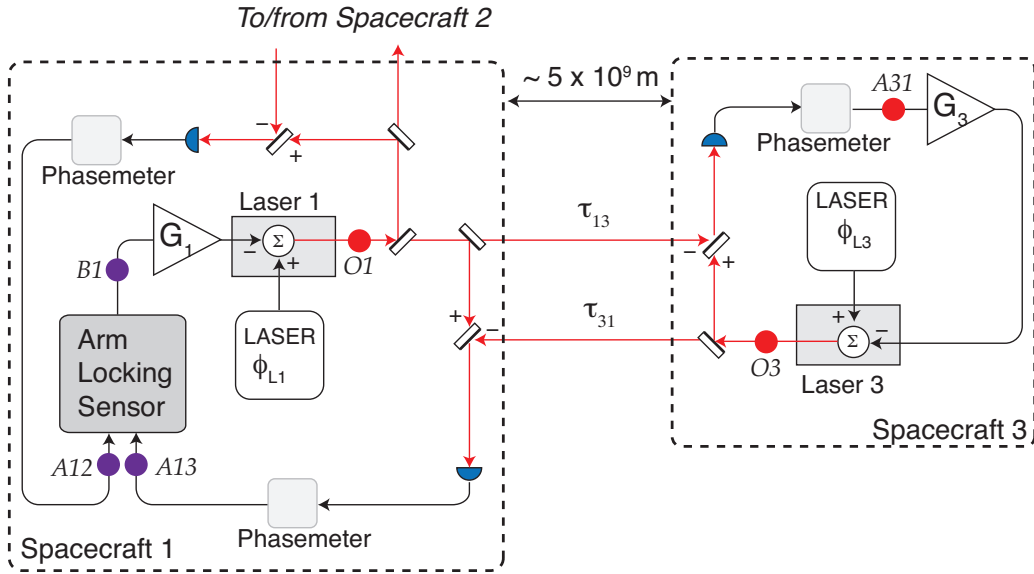


Figure 17: Schematic of arm locking control loop. Laser frequency noise is represented by ϕ_{Lj} , with j representing the number of the local spacecraft. The clock noise, shot noise, and spacecraft motion are not shown.

Figure 17 show a schematic of the arm locking control system. The phase measurements that enter the arm locking sensor on the central spacecraft (points A12 and A13) are

$$\Phi_{A1} = \begin{bmatrix} \phi_{A13} \\ \phi_{A12} \end{bmatrix} \approx \phi_{L1} \begin{bmatrix} P_{13}(\omega) \\ P_{12}(\omega) \end{bmatrix} + \mathbf{N}_S + \mathbf{N}_C + \mathbf{N}_X. \quad (17)$$

where ϕ_{A13} and ϕ_{A12} represent the phase measured on the central spacecraft in the 13 arm and 12 arm respectively, ϕ_{L1} is the laser phase noise of the laser on the central spacecraft, and $P_{13}(\omega)$ and $P_{12}(\omega)$ are the frequency responses of the 13 arm and 12 arm respectively. The vectors \mathbf{N}_S , \mathbf{N}_C , and \mathbf{N}_X contain shot noise, clock noise, and spacecraft

jitter noise [30], discussed in section 3.5. If the lasers on the far spacecraft are phased locked to the incoming light with high gain, $P_{13}(\omega)$ and $P_{12}(\omega)$ can be well approximated by [30]

$$P_{13}(\omega) \approx 1 - e^{-i2\omega\tau_{13}}, \quad P_{12}(\omega) \approx 1 - e^{-i2\omega\tau_{12}}. \quad (18)$$

where τ_{13} and τ_{12} are the one-way light propagation delays in the respective arms.

The signals in Φ_{A1} can be combined using the signal mapping vector, \mathbf{S}_k , where $k = S$ for single arm locking, $k = +$ for common arm locking, and $k = D$ for dual arm locking. The signal mapping vectors and frequency responses are given in table 4. The open loop noise at the output of the arm locking sensor (point $B1$ in Figure 17) is simply $\phi_{B1}|_k = \mathbf{S}_k \Phi_{A1}$. The frequency noise at laser output with the arm locking control loop closed (point $O1$ in Figure 17) is

$$\phi_{O1}|_k = \phi_{L1} - \frac{G_1(\omega)\phi_{B1}|_k}{1 + G_1(\omega)P_k(\omega)}, \quad (19)$$

$$= \frac{\phi_{L1}}{1 + G_1(\omega)P_k(\omega)} - \frac{G_1(\omega)}{1 + G_1(\omega)P_k(\omega)} \mathbf{S}_k \mathbf{N}, \quad (20)$$

where $G_1(\omega)$ is the gain of the arm locking controller and $P_k(\omega)$ is the frequency response of the k th sensor.

Table 4: The signal mapping vector and frequency response of different arm locking configurations. Here τ_{ij} is the one way light travel time of the ij th arm, $\bar{\tau}$ is the average round trip time of the two arms, and $E(\omega)$ is an filter used to combine the common and difference sensors, given in [30]. The parameters $H_+(\omega)$ and $H_-(\omega)$ are defined in equation 24.

Configuration	Signal Mapping	Frequency Response
Single	$\mathbf{S}_S = \begin{bmatrix} 1, & 0 \end{bmatrix}$	$P_S(\omega) = 2i \sin(\tau_{ij}\omega) e^{-i\omega\tau_{ij}}$
Common	$\mathbf{S}_+ = \begin{bmatrix} 1, & 1 \end{bmatrix}$	$P_+(\omega) = 2(1 - \cos(\Delta\tau\omega)) e^{-i\omega\bar{\tau}}$
Difference	$\mathbf{S}_- = \begin{bmatrix} 1, & -1 \end{bmatrix}$	$P_-(\omega) = -2i \sin(\Delta\tau\omega) e^{-i\omega\bar{\tau}}$
Dual	$\mathbf{S}_D = \begin{bmatrix} 1 - \frac{E(\omega)}{i\omega\Delta\tau}, & 1 + \frac{E(\omega)}{i\omega\Delta\tau} \end{bmatrix}$	$P_D(\omega) = P_+(\omega) - \frac{E(\omega)}{i\omega\Delta\tau} P_-(\omega)$
Modified dual	$\mathbf{S}_M = \begin{bmatrix} H_+(\omega) - H_-(\omega), \\ H_+(\omega) + H_-(\omega) \end{bmatrix}$	$P_M(\omega) = P_+(\omega)H_+(\omega) - P_-(\omega)H_-(\omega)$

3.3 Modified Dual Arm Locking

A combination of common and dual arm locking sensors can be used to retain the control system advantages of dual arm locking and minimize frequency pulling and low frequency

noise. This modified dual arm locking sensor is designed so that the common arm sensor dominates below the first null of the arm ($f < 1/\bar{\tau}$) and the dual sensor dominates above this frequency [30]. The components of the modified sensor are plotted in Figure 18. The frequency response of the sensor is

$$P_M(\omega) = \underbrace{F_C(\omega)P_+(\omega)}_{\text{Common Part}} + \underbrace{F_D(\omega)P_D(\omega)}_{\text{Dual Part}}, \quad (21)$$

where the functions $F_C(\omega)$ and $F_D(\omega)$ are filters designed to smooth the crossover from the common to dual sensors given by

$$F_C(\omega) = \frac{g_a g_b (s + z_b)}{s(s + p_b)}, \quad F_D(\omega) = \frac{g_c g_d g_e s^4}{(s + p_c)(s + p_d)(s + p_e)^2}, \quad (22)$$

with the parameters given in table 5. Equation 21 can be rewritten as a function of the

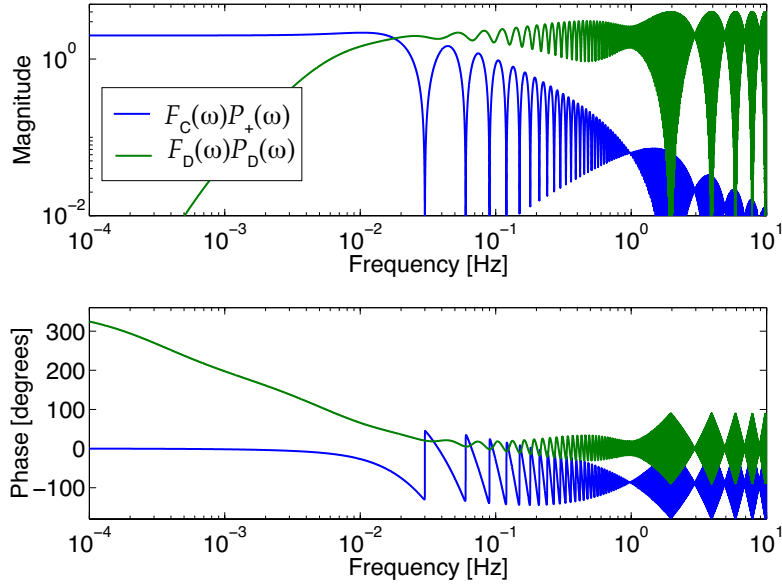


Figure 18: Common and dual components of the modified dual arm locking sensor. The combination of these gives the modified dual arm locking sensor.

common and difference sensors

$$P_M(\omega) = P_+(\omega)H_+(\omega) - P_-(\omega)H_-(\omega), \quad (23)$$

with

$$H_+(\omega) = F_C(\omega) + F_D(\omega), \quad H_-(\omega) = \frac{E(\omega)}{i\omega\Delta\tau}F_D(\omega). \quad (24)$$

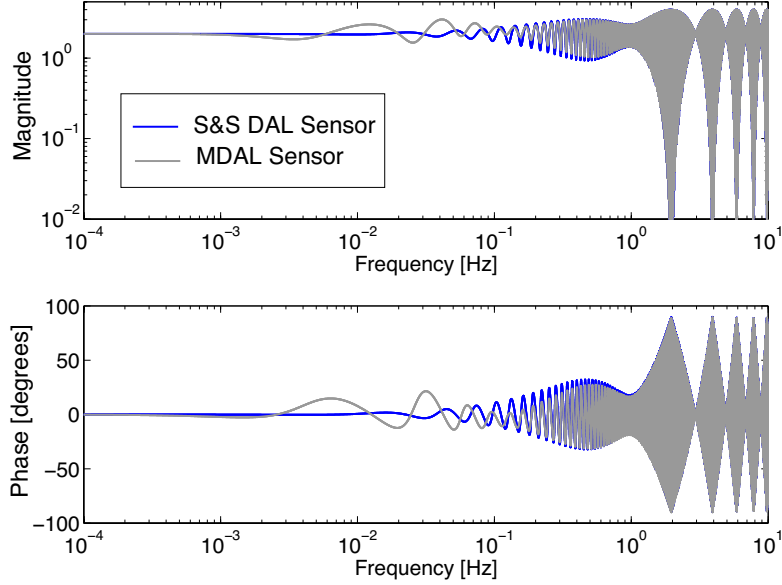


Figure 19: Bode plot of the modified dual arm locking sensor (grey curve) and the Sutton and Shaddock [21] (S&S) dual arm locking sensor (blue curve).

The frequency response of the modified dual arm locking sensor, shown in Figure 19, is similar to the dual arm locking sensor, with an almost flat response below the first null with a magnitude of 2.

Table 5: Parameters of modified dual arm locking filters

Filter	zeros (radians/s)	Poles (radians/s)	Gain
$F_C(\omega)$	$z_b = 2\pi \times 5/(13\bar{\tau})$	$p_a = 0$ $p_b = 2\pi \times 5/(2\bar{\tau})$	$g_a = (\bar{\tau})^{-1}$ $g_b = p_b/z_b$
$F_D(\omega)$	0 0 0	$p_c = 7/(5\bar{\tau})$ $p_d = 11/(20\bar{\tau})$ $p_e = 2\pi \times 1/(90\bar{\tau})$	$g_c = 1$ $g_d = 1$ $g_e = 1$

3.4 Laser Frequency Pulling

The relative velocities of the spacecraft cause a Doppler shift of up to 18 MHz [32]. For arm locking to operate stably, this round trip Doppler frequency must be estimated and subtracted in the phase measurements used in the arm locking sensor. In the limit of

a high gain DC coupled arm locking control system, an error in the estimated Doppler frequency is compensated for by changing the local laser frequency to maintain the desired beat note frequency. In single arm locking, this frequency change will appear on the light returning from the distant spacecraft 33 s later, necessitating a further change by the local laser frequency to maintain the desired beat note frequency. The closed loop master laser frequency, ν_{CL} , will be changed by the error in the Doppler frequency, ν_{DE} , each round trip, or an average rate of $\frac{\delta\nu_{\text{CL}}}{\delta t} = \nu_{\text{DE}} \frac{c}{2L}$ Hz/s. For example, if the Doppler frequency can be estimated to 100 kHz, the laser frequency will be forced to change by 1 GHz in 4 days. Such large pulling of the laser frequency is undesirable, as it could drive the master laser through a mode-hop region, compromising instrument sensitivity. The other lasers in the constellation are also at risk of being pulled into a mode-hop region as they will be locked to the master laser frequency. Additionally, ramping of laser frequency combined with scattered light sources can couple noise into the science band, see Section 4.7.

Frequency pulling can be considered in two regimes: 1) in steady state operation, and 2) at lock acquisition. At lock acquisition, the laser frequency can be pulled significantly by an error in the initial Doppler frequency estimate and also in the time derivatives of the Doppler frequency. We see two solutions:

- Add high pass filters to the arm locking control loop to limit this.
- Have a DC coupled controller with an additional control loop operating at low frequencies to limit the amplitude of the controller signal at these frequencies [31].

While we present the first solution here, the second, active solution may have precision advantages in implementation and details can be found in reference [31].

We expect the arm locking control system will operate as follows: before arm locking is engaged, measurements of the Doppler frequency and the Doppler rate (the first time derivative of the Doppler frequency) will be made (Appendix A. of reference [30]) and subtracted from the phasemeter measurement. After the control loop is closed, the error in the Doppler frequency measurement will cause the laser frequency to ramp at a rate proportional to the product of the error and the step response of the controller. Whilst locked, the Doppler frequency estimate will not need to be updated. The arm locking control loop will be unlocked and re-locked periodically to perform mission tasks, such as to change the heterodyne frequencies [32]. At these times the Doppler frequency and its time derivatives will be known very accurately (as many weeks or months of data can be averaged to measure it) and the impulse to laser frequency will be much smaller than in the first time arm locking is engaged.

3.4.1 Pulling in Steady State

The laser frequency pulling in modified dual arm locking arises due to both the common, $\nu_{\text{DE}+} = \nu_{\text{DE}12} + \nu_{\text{DE}13}$, and differential errors, $\nu_{\text{DE}-} = \nu_{\text{DE}12} - \nu_{\text{DE}13}$ in the Doppler

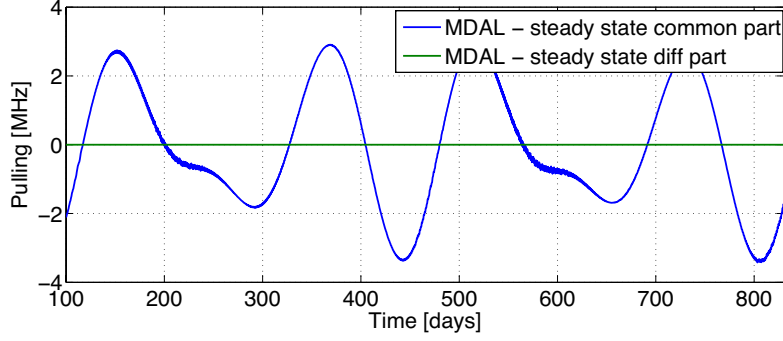


Figure 21: The laser frequency pulling when arm locking is engaged. The pulling arises because the changing Doppler frequencies. The component due to the common Doppler shift dominates.

frequency². Thus, the first and second time derivatives of the Doppler frequency, labeled $\gamma_+(t)$, and $\alpha_+(t)$, need to be accounted for. The common Doppler frequency error in the time domain is

$$\nu_{\text{DE}+}(t) = \nu_{0+} + \int_0^t \gamma_+(t) dt + \int_0^t \int_0^{t'} \alpha_+(t) dt' dt +$$

(Higher order terms), (27)

Higher order time derivatives of the common Doppler frequency error are neglected because they are sufficiently small.

The design of the arm locking controller is such that the transients will decay over a period of a few days. Over this period the terms $\gamma_+(t)$, $\alpha_+(t)$ will change little and for simplicity we shall approximate these terms as constants equal to their initial errors. The Doppler error at lock acquisition is then

$$\nu_{\text{DE}+}(t) \approx \nu_{0+} + \gamma_{0+}t + \frac{\alpha_{0+}t^2}{2}, \quad (28)$$

with the initial errors in the Doppler rate, change in the Doppler rate given by γ_{0+} and α_{0+} . In the frequency domain, the Doppler error at lock acquisition is

$$\nu_{\text{DE}+} \approx \nu_{0+} + \frac{\gamma_{0+}}{i\omega} - \frac{\alpha_{0+}}{2\omega^2}. \quad (29)$$

²The errors in the differential Doppler frequency can be neglected for modified dual arm locking [30]

The frequency responses to the different terms in equation 29 can be found using equation 25. The frequency responses are

$$\mathcal{V}^{(+)}(\omega) = \frac{-G_1(\omega)H_+(\omega)}{1 + G_1(\omega)P_M(\omega)}, \quad (30)$$

$$\mathcal{G}^{(+)}(\omega) = \frac{-G_1(\omega)H_+(\omega)}{i\omega(1 + G_1(\omega)P_M(\omega))}, \quad (31)$$

$$\mathcal{A}^{(+)}(\omega) = \frac{G_1(\omega)H_+(\omega)}{2\omega^2(1 + G_1(\omega)P_M(\omega))}. \quad (32)$$

Frequency pulling during lock acquisition is determined by the step response of the control system. The step response follows from the closed-loop control system $\nu_{\text{CL}}(s)$ according to

$$\nu_{\text{step}}(t) = \mathcal{L}^{-1} \left(\frac{\nu_{\text{CL}}(s)}{s} \right), \quad (33)$$

where $s = i\omega$ and \mathcal{L}^{-1} is the inverse Laplace transform operator. Step responses from the error in the three Doppler derivatives, equations 30-32, are plotted in Figure 22, for both free-running and pre-stabilized lasers. The maximum pulling including errors in all the derivatives of ν_{0+} is 460, 90, and 4 MHz, for the respective cases of free-running, Mach-Zehnder pre-stabilized, and Fabry-Perot cavity pre-stabilized lasers. These plots have been made assuming 200 s of averaging for the Doppler estimates and show that since the Doppler frequency estimates are better for pre-stabilized lasers, the pulling is smaller. Further reduction of pulling can be achieved simply by increasing the Doppler frequency measurement time. In the case of free-running laser noise, the estimates of γ_{0+} and α_{0+} have an error larger than the maximum value determined by the orbital motion. Thus we do not use the laser measurement of these quantities; rather, we assume them to be zero. With pre-stabilization the error in the measurement of α_{0+} is larger than its maximum value and thus we assume it to be zero.

3.5 Noise Limits

For modified dual arm locking, the noise at the laser output is

$$\phi_{O1}|_M = \frac{\phi_{L1}}{1 + P_M(\omega)G_1(\omega)} - \frac{G_1(\omega)}{1 + P_M(\omega)G_1(\omega)} \mathbf{S}_M [\mathbf{N}_S + \mathbf{N}_C + \mathbf{N}_X], \quad (34)$$

The vectors containing the shot noise, clock noise, and spacecraft motion are given by

$$\begin{aligned} \mathbf{N}_S &= \begin{bmatrix} \phi_{S12} + \phi_{S21} \\ \phi_{S13} + \phi_{S31} \end{bmatrix}, \mathbf{N}_C = \begin{bmatrix} \frac{\Delta_{12}}{2\pi f} (y_1(f) + y_2(f)) \\ \frac{\Delta_{13}}{2\pi f} (y_1(f) + y_3(f)) \end{bmatrix}, \\ \mathbf{N}_X &= \begin{bmatrix} \phi_{X12} (1 + e^{-i2\omega\tau_{12}}) + 2\phi_{X21} \\ \phi_{X13} (1 + e^{-i2\omega\tau_{13}}) + 2\phi_{X31} \end{bmatrix}. \end{aligned} \quad (35)$$

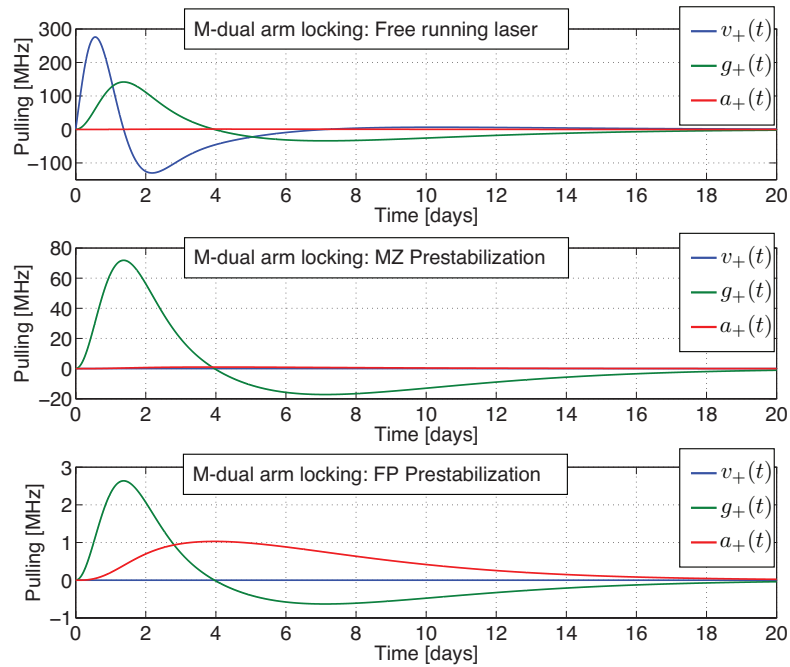


Figure 22: The step responses of different drivers of Doppler frequency error for modified dual arm locking. The upper, middle, and lower plots assume free-running laser noise, Mach-Zehnder type pre-stabilization, and Fabry-Perot cavity pre-stabilization, respectively, with the Doppler frequency estimates averaged for 200 s.

3.5.1 Performance Assuming Free-running Laser Noise

Figure 23 shows the noise budget of modified dual arm locking (plotted using equation 34) with free-running laser noise, an arm length mismatch of $2\Delta\tau = 0.51$ s, and the parameters in table 6. The total noise (dashed black curve) is a quadrature sum of shot noise (red curve), spacecraft motion (green curve), the clock noise (blue curve) and laser frequency noise (cyan curve). For this arm length mismatch the laser frequency noise is the limiting noise source (the system is gain limited) with the other system noise sources well below the laser frequency noise. Clock noise is the largest other noise source below 20 mHz and spacecraft motion represents a noise limit at frequencies above this. Note that clock noise is linearly dependent on the heterodyne frequency at each phasemeter and this plot was made with the worst combination of heterodyne frequencies that can occur for dual arm locking: a maximum difference in Doppler shifts between the two arms, $\Delta_{13} - \Delta_{12} = 29$ MHz. In the science band, shot noise is always smaller than the both clock and spacecraft motion, though it dominates above band as clock noise and spacecraft motion roll off.

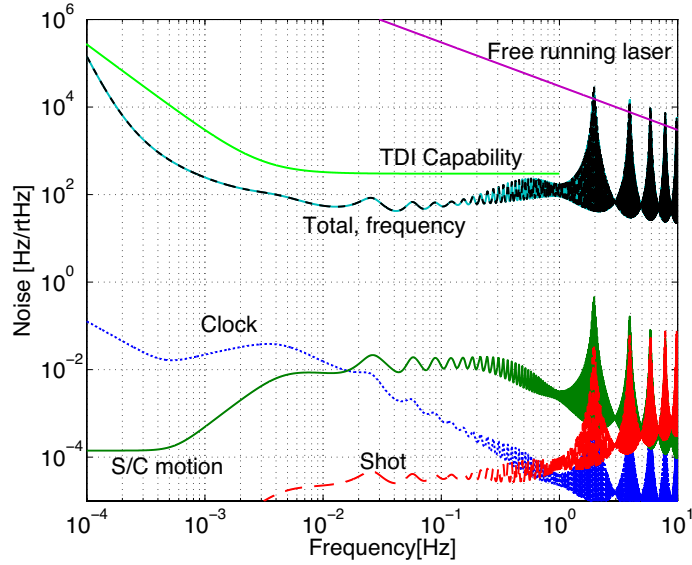


Figure 23: The noise budget of modified dual arm locking with arm length mismatch of $\Delta\tau = 0.51$ s. The performance was calculated with free-running laser noise as an initial condition.

Even without any form of laser pre-stabilization arm locking will meet the TDI capability across the entire LISA science band. At the most sensitive frequency of LISA, 3 mHz the frequency noise is a factor of 5 below the TDI capability. If there is not a failure of one inter-spacecraft laser link, the dual arm locking central spacecraft can be switched when the arm length mismatch becomes small, and arm locking alone has sufficient performance

to meet the TDI capability for the mission.

The variation of the modified dual arm locking noise floor due to the changing arm length mismatch can be seen in Figure 24. This shows the noise sources at 3 mHz over the first two years of the LISA mission assuming only two of the three LISA arms are available. In this case, the noise floor at 3 mHz is below the TDI capability for the vast majority of the time and breaches the TDI capability for only short periods, twice per year. It also provides some indication of how infrequently and how short a time dual arm locking can not meet the TDI capability in case of a critical failure of one arm. The noise performance is insufficient to meet the TDI capability for approximately 1/2 an hour, twice per year.

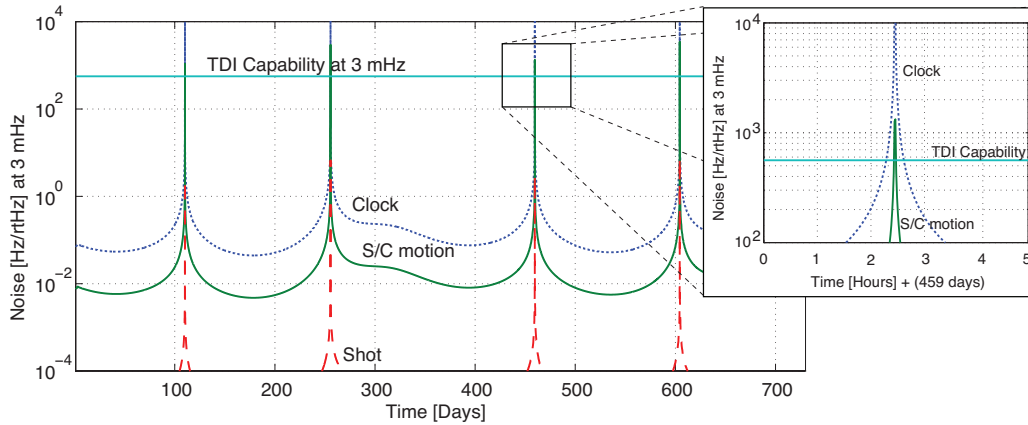


Figure 24: The noise sources of arm locking measured at 3 mHz over the first two years of the LISA mission. This plot assumes only two of the three LISA arms are available, preventing the central spacecraft from being switched at small arm length mismatch. The heterodyne frequency assumed for the clock noise curve here is pessimistic, as we have assumed the worst case that occurs in the mission ($\Delta_{12} - \Delta_{13} = 29$ MHz) for the duration of this plot. The heterodyne frequency over the mission lifetime depends on the Doppler shift, which we have neglected for simplicity.

3.6 The Arm Locking Controller

The arm locking controller is designed for the modified dual arm locking sensors. Compared to a standard phase-locking control loop, the arm locking control loop has two additional design constraints. These are:

1. The controller should have appropriate low frequency filtering to limit the laser frequency pulling.
2. The controller must allow for the nulls in the sensor and the additional phase delay associated with them. The nulls in the dual arm locking sensor occur at frequencies

Table 6: LISA parameters and amplitude of noise sources

Parameter	Symbol	Value	Units
Average arm length	\bar{L}	5×10^9	m
Differential arm length	ΔL	$\leq 76,500,000$	m
Laser wavelength	λ	1064	nm
Doppler shift arm 13	Δ_{13}	15	MHz
Doppler shift arm 12	Δ_{12}	-14	MHz
Fluctuations of clock	$y(f)$	$2.4 \times 10^{-12}/\sqrt{f}$	$1/\sqrt{\text{Hz}}$
Shot noise	ϕ_{Sij}	10	$\mu\text{cycles}/\sqrt{\text{Hz}}$
Spacecraft motion	ϕ_{Xij}	$2.5 \times \sqrt{1 + (f/0.3\text{Hz})^4}$	$10^{-3} \cdot \text{cycles}/\sqrt{\text{Hz}}$
TDI capability	$\nu_{\text{TDI}}(f)$	$300 \times (1 + (3 \text{ mHz}/f)^2)$	$\text{Hz}/\sqrt{\text{Hz}}$

above 2 Hz.

These additional constraints limit the achievable gain in the LISA science band and necessitate careful design to ensure loop stability. Although the controller is designed for the maximum arm length mismatch, it will operate stably for smaller arm length mismatch.

3.6.1 Controller Overview

A block diagram of the controller architecture is shown in Figure 25. The controller consists of five stages. Stage 1 is the very low frequency part of the controller and comprises three zero-pole pairs to form unity gain high pass filters at $0.8 \mu\text{Hz}$ in series. Stage 2 sets the lower unity gain frequency and has a zero at DC and a pole at $210 \mu\text{Hz}$. This low frequency filtering is adopted to limit laser frequency pulling that arises at lock acquisition and in steady state. Stage 3 is a lead stage, which has five zero-pole stages in series to roll up the gain steeply between the lower unity gain frequency and the low frequency part of the controller. Stage 4 consists of two poles in series and provides the transition between the low frequency gain and the shallow slope high frequency part of the controller. Stage 5 is the shallow sloped part of the controller. It consists of nine poles in parallel, with the gain for each pole chosen to achieve the required slope of approximately $f^{-0.66}$ a slope optimized to maximize the gain while maintaining > 30 degree phase margin at the unity gain frequencies. The frequency response of the controller is given by

$$G_1^*(\omega) = \left(\frac{g_1 s}{s + p_1} \right)^3 \left(\frac{g_2 s}{s + p_2} \right) \left(\frac{g_3(s + z_3)}{s + p_3} \right)^5 \left(\frac{g_4}{(s + p_{41})(s + p_{42})} + \sum_{k=1}^9 \frac{g_{5k}}{s + p_{5k}} \right), \quad (36)$$

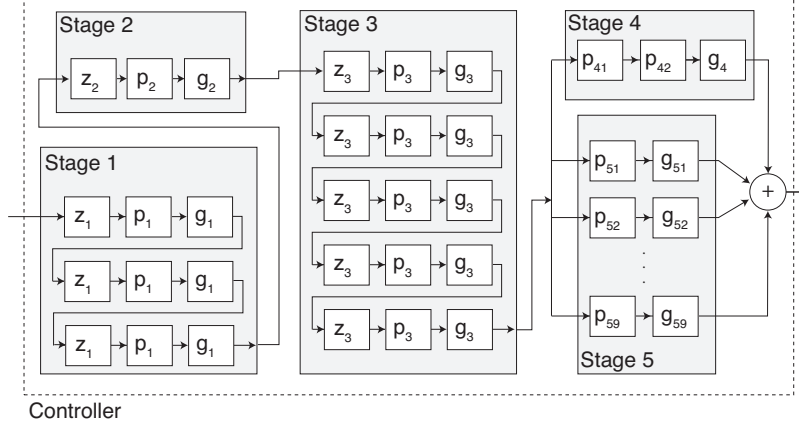


Figure 25: Block diagram of the arm locking controller. The controller is built from five stages: stage 1 consist of three very low frequency high pass filters, stage 2, defines the lower unity gain frequency; stage 3, rolls up the gain below the LISA science band; stage 4 has two poles in parallel to effectively transition between stage 3 and stage 5; stage 5 has 9 poles in parallel, with gains individually chosen to generate a slope of approximately $f^{-0.66}$.

with values of the zeros, poles, and gains listed in table 7³.

The assumption of delays in the control system are shown in table 8. The open loop gain of the control system with the modified dual arm locking sensor is given by

$$G_L(\omega) = G_1(\omega)P_M(\omega)e^{-i\omega(\tau_{act} + \tau_{pm} + \tau_{trans} + \tau_{ps})}. \quad (37)$$

The Bode plot of $G_L(\omega)$ is plotted in Figure 26. Note that in this plot we have assumed the phase delays of the pre-stabilization control loop can also be removed and thus set $\tau_{ps} = 0$. Thus, when we discuss system options in section II the same arm locking controller can be used with and without pre-stabilization.

The open loop phase looks somewhat deceptive. At high frequencies it appears that the open loop phase crosses 180 degrees before 1 kHz, making the 14.9 kHz bandwidth control loop unstable. In fact, the total phase at the unity gain points is always greater than -150 degrees which is indicated by the red solid curve, which is given by

$$\theta_{UG} = \angle G_1^*(\omega) \times \frac{180}{\pi} + \theta_{sensor|UG} + 360f(\tau_{act} + \tau_{pm} + \tau_{trans}), \quad (38)$$

which is valid for $f \geq 1/(2\Delta\tau)$.

³An additional low pass filter in series with the controller is generally required to roll off the loop gain at the resonance frequency of the laser PZT actuator (near 100 kHz)

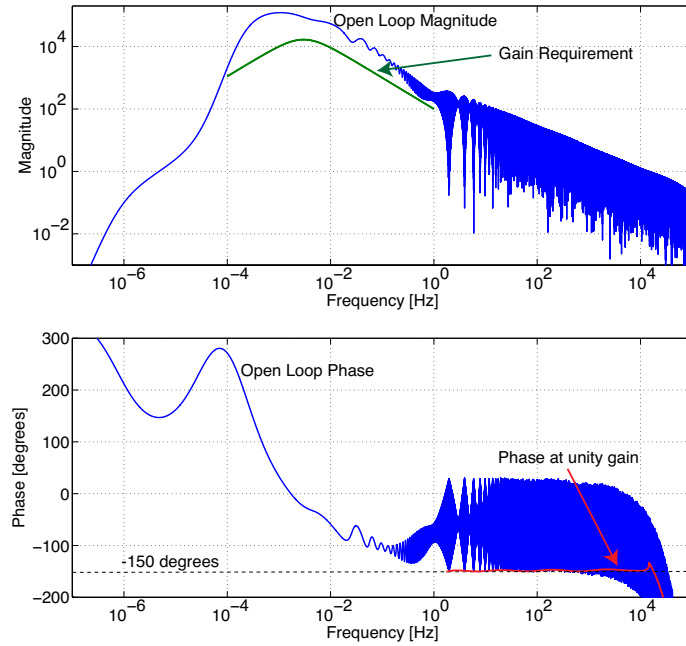


Figure 26: Open loop frequency response, $G_L(\omega)$, of modified dual arm locking. Also shown in the magnitude plot is the gain required to meet the TDI capability, assuming no pre-stabilization. In the phase plot, the red curve indicates the total phase of the control loop at unity gain (given by equation 38). The arm length mismatch is assumed to be $2\Delta\tau = 0.51\text{s}$.

Table 7: Parameters of the arm locking controller

Stage	zeros (radians/s)	Poles (radians/s)	Gain (radians/radian)
1	$z_1 = 0$	$p_1 = 2\pi \times 8 \times 10^{-7}$	$g_1 = 1$
2	$z_2 = 0$	$p_2 = 2\pi \times 210 \times 10^{-6}$	$g_2 = 0.95/f_{ac}$
3	$z_3 = 2\pi \times 36.6 \times 10^{-6}$	$p_3 = 2\pi \times 185 \times 10^{-6}$ ⁴	$g_3 = p_3/z_3$
4		$p_{41} = 2\pi \times 3 \times 10^{-3}$ $p_{42} = 2\pi \times 238 \times 10^{-3}$	$g_4 = p_{41}p_{42}$
5		$p_{51} = 2\pi \times 3 \times 10^{-3}$ $p_{52} = 2\pi \times 3 \times 10^{-2}$ $p_{53} = 2\pi \times 3 \times 10^{-1}$ $p_{54} = 2\pi \times 3$ $p_{55} = 2\pi \times 3 \times 10^1$ $p_{56} = 2\pi \times 3 \times 10^2$ $p_{57} = 2\pi \times 3 \times 10^3$ $p_{58} = 2\pi \times 3 \times 10^4$ $p_{59} = 2\pi \times 3 \times 10^5$	$g_{51} = 1.3 \times 10^{-3}$ $g_{52} = 3.7 \times 10^{-3}$ $g_{53} = 4.2 \times 10^{-3}$ $g_{54} = 16 \times 10^{-3}$ $g_{55} = 30 \times 10^{-3}$ $g_{56} = 69 \times 10^{-3}$ $g_{57} = 0.11$ $g_{58} = 0.33$ $g_{59} = 0.70$

The disturbance suppression function is shown in Figure 27. Also plotted is the required suppression to meet the TDI capability. Note that the amplification at the nulls is always less than a factor of 2 except near the final unity gain frequency, near 15 kHz, where the amplitude increases to 5.

3.7 Summary

Our understanding of arm locking has matured significantly in the last year. We have:

- A detailed analysis of arm locking which includes many of the orbital effects expected on LISA.
- Understanding of laser frequency pulling and two methods to limit to an acceptable level.
- A noise analysis includes the expected dominant noise sources in arm locking; clock noise, spacecraft motion, and shot noise.
- A new sensor design for the dual arm locking sensor that uses a combination of the common and dual arm sensor at frequencies below $1/\bar{\tau}$ and the dual arm locking sensor frequencies above $1/\bar{\tau}$ to retain the control system advantages of dual arm locking while inheriting the frequency pulling characteristics and low frequency noise performance of common arm locking.

Table 8: Arm locking system delays

Type of Delay	Symbol	Delay	Notes
Arm locking sensor	$\theta_{sensor UG}$	$-\arccos\left(\frac{1}{ 2G_1^*(\omega) }\right)$	Phase at unity gain [30]
Actuator delay	τ_{act}	$5\mu s$	PZT delay ($4\mu s$ measured)
Phasemeter	τ_{pm}	$2\mu s$	DACs have $1\mu s$ delay
Transponding S/C	τ_{trans}	$(2\pi 30kHz)^{-1}s$	30kHz UGF assumed ⁵
Pre-stabilization	τ_{ps}	$(2\pi 30kHz)^{-1}s$	30kHz UGF assumed

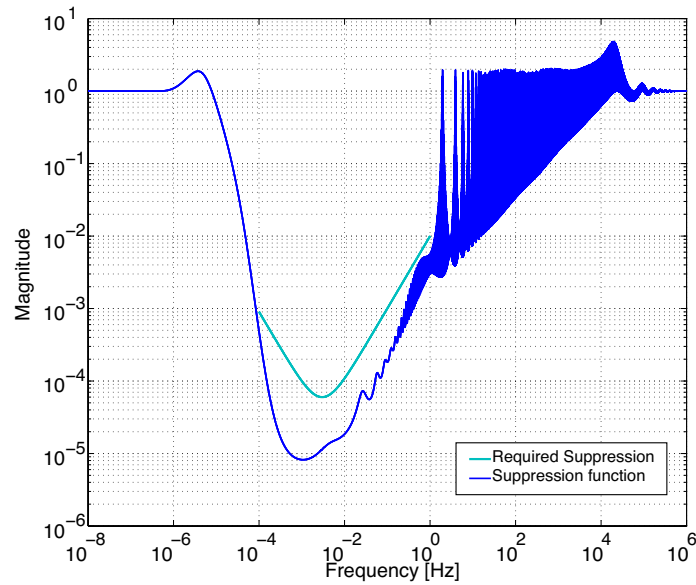


Figure 27: Plot of the disturbance sensitivity, $S_D(\omega) = 1/(1 + G_L(\omega))$ and the required suppression to meet the TDI capability without pre-stabilization. Plotted with $2\Delta\tau = 0.55s$.

- A detailed controller designed to maximize gain in the science band, minimize frequency pulling, but still maintain a phase margin of greater than 30 degrees to ensure stability. The control bandwidth (~ 15 kHz) is 10 times higher than previously expected possible.

4 Time-Delay Interferometry

The final step in frequency noise suppression is a post-processing technique called Time-Delay Interferometry (TDI) [33]. TDI removes laser frequency noise by forming linear combinations of the phase measurements with different delays. TDI can be understood as a way to synthesize an interferometer that has equal arm lengths. To achieve this, phase measurements recorded locally at each spacecraft are time shifted using high performance interpolation algorithms and recombined in post-processing. These same linear combinations maintain the gravitational wave signal, as it is primarily contained in the difference of the arms while the laser noise is common to the arms.

The performance of TDI can be characterized by a suppression factor. Here we define the suppression factor to be the ratio of laser frequency noise to the frequency noise remaining in the TDI output. This suppression factor is frequency dependent and may be limited by several effects. Six categories of these effects are listed Table 9 along with an estimate of the suppression factor limit due to each effect.

Table 9: Effects that limit the TDI suppression factor.

Effect	Assumption	Suppression Factor
Ranging Error	1 m ranging error	$2.4 \times 10^7 \times (1 \text{ Hz}/f)$
Algorithm limitations	Velocity correcting TDI	$2 \times 10^9 \times (1 \text{ Hz}/f)$
Interpolation	21 s kernel, 3 S/s	$3.2 \times 10^9 \times (1 \text{ Hz}/f)^2$
Analog Chain Errors	Measurement	$5 \times 10^7 \times (1 \text{ Hz}/f)$
Phasemeter DSP	TRL 4 Phasemeter	$10^{10} \times (1 \text{ Hz}/f)^2$
Scattered Light	Amplitude 2×10^{-5}	$1.5 \times 10^{13} \times (1 \text{ Hz}/f)$

4.1 Ranging Limited Performance

In this section we determine the suppression factor of TDI due to ranging error. This calculation is based on the LISA technical note *TDI Capabilities and Frequency Noise Requirements* [34].

Time-Delay Interferometry processing affects not just laser frequency noise but all other noise sources and the gravitational wave signal. We need to consider this response when

determining the requirements on laser frequency noise suppression. For example, it is not sufficient to require that the laser frequency noise after TDI is less than the shot noise level before TDI. Instead we require that the laser frequency noise after TDI is less than the shot noise after TDI. The frequency noise allocation post TDI, $\phi_{ln|TDI}$, can be written as a fraction of shot noise.

$$\phi_{ln|TDI} = KT_{sn}(f)\phi_{sn|PR} \quad (39)$$

where K is the fraction of the shot noise level allocated to residual laser frequency noise, $T_{sn}(f)$ is the frequency response of shot noise into the TDI output, and $\phi_{sn|PR}$ is the sum of shot noise and acceleration noise at the photoreceiver, given by

$$\phi_{sn|PR} = \frac{7.5\text{pm} \times \sqrt{1 + (3\text{mHz}/f)^4}}{\lambda} \text{ cycles}/\sqrt{\text{Hz}}. \quad (40)$$

where λ is the laser wavelength.

The allowable laser frequency noise pre-TDI is found by dividing the allocation (equation 39) by the frequency response for frequency noise, $T_{ln}(f)$, and converting from phase to frequency.

$$\nu_{ln|LAS} = \left(\frac{2\pi f}{\lambda} \right) \frac{T_{sn}(f)}{T_{ln}(f)} K x_{sn|PR}. \quad (41)$$

To get a feel for the numbers we can substitute numbers in for the laser noise allocation $x_{ln|PR} = K x_{sn|PR}$ and ranging errors. If we assume the TDI combination X [33] (the Michelson interferometer combination), with $\Delta L = 1$ m error and $x_{ln|PR} = 1$ pm/ $\sqrt{\text{Hz}}$ we find

$$\nu_{ln|LAS} = 141 \text{ Hz}/\sqrt{\text{Hz}} \times \left(\frac{1\text{m}}{\Delta L} \right) \times \left(\frac{x_{ln|PR}}{1 \text{ pm}/\sqrt{\text{Hz}}} \right). \quad (42)$$

where we have assumed the worst case of frequency noise coupling, which occurs with a differential ranging error coupled with matched arm lengths. Equation 42 shows the suppression of frequency noise by TDI depends linearly on the accuracy of the arm length knowledge or ranging error. A TDI suppression factor of $2.4 \times 10^7 \times (1 \text{ Hz}/f)$ is possible with 1 m ranging error.

The frequency responses in equation 41 are specific to the TDI combination chosen. The frequency response of shot noise into the (first generation) TDI combination X is

$$T_{sn}(f) = \sqrt{2} \sqrt{(1 - e^{-i\omega 2L_{2E}/c})^2 + (1 - e^{-i\omega 2L_{1E}/c})^2}, \quad (43)$$

where L_{1E}, L_{2E} are the estimated lengths of the two arms given by $L_{1E} = L_1 + \Delta L_1$, $L_{2E} = L_2 + \Delta L_2$, with L_1 and L_2 denoting the actual arm lengths of the two LISA arms and ΔL_1

and ΔL_2 denoting the ranging error for the respective arms. The frequency response of laser frequency noise for the TDI combination X is

$$T_{ln}(f) = T_{arm1}(f) \left(1 - e^{-i\omega 2L_{2E}/c}\right) - T_{arm2}(f) \left(1 - e^{-i\omega 2L_{1E}/c}\right), \quad (44)$$

where $T_{arm1}(f)$ and $T_{arm2}(f)$ are the frequency responses of the arms 1 and 2, given by

$$T_{arm1}(f) = 1 - e^{-i\omega 2L_1/c}, \quad T_{arm2}(f) = 1 - e^{-i\omega 2L_2/c}. \quad (45)$$

The frequency responses of laser frequency noise and shot noise are different because they

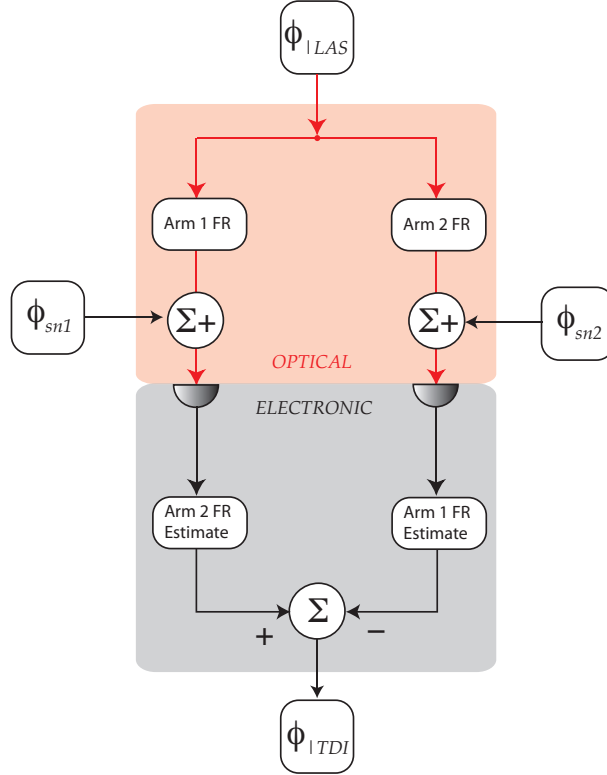


Figure 28: Block diagram representation of TDI showing where the laser frequency noise, ϕ_{ln} and the shot noise, ϕ_{sn} enter the signal chain. The frequency responses (FR) of the arms are applied in the post processing stage of TDI.

enter the signal chain at different locations: laser frequency noise enters at the laser, shot noise enters at the photoreceiver. This is shown schematically in Figure 28 for the case of the TDI combination X . For simplicity it is assumed that the lasers are perfectly phase-locked to one master laser in the central spacecraft. The electronic processing part of the diagram depicts the formation of the TDI combinations performed on ground.

The frequency noise requirement calculated for 2nd generation TDI is the same as 1st generation TDI [34].

4.2 Ranging System

TDI relies on interspacecraft distance tracking with resolution on the order of meters as described in section 4.1. The LISA interferometry system will provide onboard ranging measurements and data communication by applying low-index phase modulation onto all laser links. To achieve the required distance accuracy, a pseudo-random noise (PRN) can be phase modulated onto the carrier of the remote laser and the travel time can be measured via the correlation of the local and incoming PRN code. To obtain the phase signal of the laser beam the beatnote coming from the photodetectors on the optical benches will be processed in a phase measurement system (PMS). Once the interference has been acquired (this constitutes the core processing of the phasemeter), the PRN can be tracked in back-end processing using the fast residual phase error as input signal. This section is based on Technical Note LI-AEI-TN-3013b [35].

4.2.1 Interfaces with the Phasemeter

The core processing of the PMS is based on a digital phase-locked loop (DPLL) [36] architecture. It is required to track the Doppler-shifted carrier (frequency range between 2 to 18 MHz) and to measure the phase of the beat note at microcycle/ $\sqrt{\text{Hz}}$ phase precision. The ranging capabilities are based on a delay-locked loop (DLL)[37] architecture. It is used to track the received PRN code and therefore the estimation of the time delay between PRN sequences can be obtained as well as the data transmitted. To focus on ranging capabilities it is assumed that the core processing of the phasemeter keeps the incoming tone in closed loop operation and a PRN sequence encoded with data have been modulated onto the incoming carrier.

The ranging system has to be integrated in or very close to the PMS. The input signal of the DLL is a high rate phase component obtained as residual of the in-phase (I) sampled signal. Figure 29 shows the schematic of one PMS channel and the proposed integration with the DLL. There may be a low-pass filter before to the DLL to minimize out-of-band interferences and additional noise. The output of the ranging system is a regular time-series of time-stamps to be processed by the onboard computer.

4.2.2 Correlation Properties of PRN Codes

There are a total of six laser beams exchanged between the LISA satellites, and therefore a PRN code has been designed for each one of them. In the LISA topology, each laser is used simultaneously in different interferometric measurements, so that it also has different codes modulated onto its phase. The main design driver for the code is that after the interference

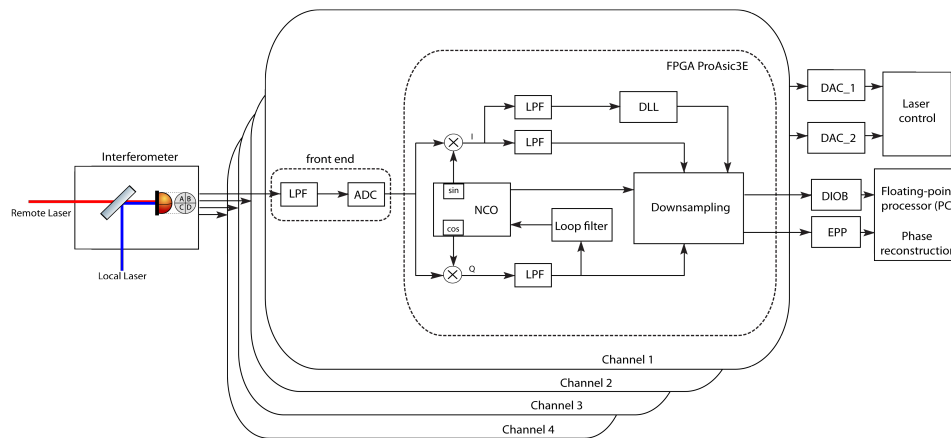


Figure 29: General PMS block diagram. FPGA: Field programmable gate array, ADC: Analog to digital converter, DAC: Digital to analog converter, LPF: Low pass filter, NCO: Numerically controlled oscillator, DLL: Delay-locked loop, DIOB: Digital input/output board, EPP: Enhanced parallel port.

between any given two lasers, a beat note can track a single PRN code separately from each other and without incurring significant mutual interference between pseudo-sequences. The set of six PRN sequences implemented shown in Figure 30 have even length (for efficient use in a FPGA processor) and have been obtained by means of numerical optimization. Note that only when the cross-correlation is made by the same PRN code with the same delay, does a peak appear in the correlation (see Figure 31). This way, the correlation peak serves as a timestamp if the start of the PRN is synchronized with the clock of the remote spacecraft.

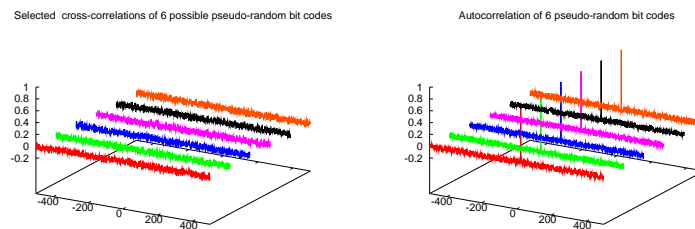


Figure 30: Cross-correlation (left) and auto-correlation (right) between a possible set of different PRN combinations

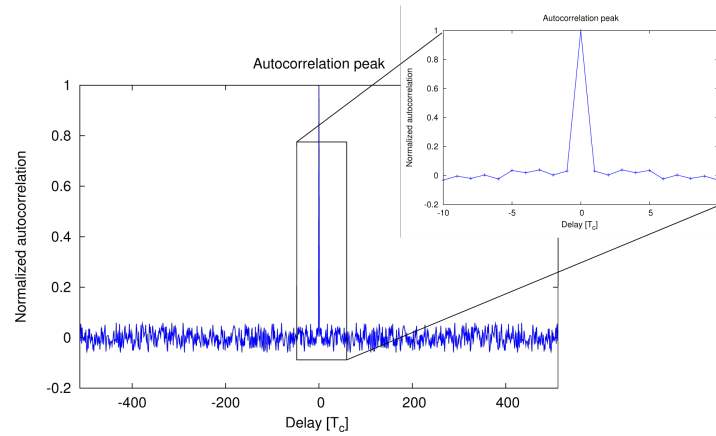


Figure 31: Autocorrelation at different code shifts and zoom at zero shift.

4.2.3 Tracking Architecture

Figure 32 shows a general block diagram of the current implementation of the code tracking part of the DLL. Sampling frequency at 50 MHz. PRN length 1024 chips at $F_c = \frac{F_s = 50 \text{ MHz}}{32 \text{ samples}} = 1.5625 \text{ MHz}$. Data encoded at $F_d = \frac{F_s = 50 \text{ MHz}}{512 \text{ samples}} = 97.65625 \text{ kHz}$

- The loop filter is updated every integration time and implemented as a first order IIR. filter:

$$\tau[n] = \tau[n - 1] + \text{gain} (E - L) \rightarrow y_i = y_{i-1} + \alpha \epsilon_i \quad (46)$$

- The code generator is implemented using one index generator and three lookup table: On-time $p(t - \tau)$, early $p(t - \tau + Tc/2)$ and late $p(t - \tau - Tc/2)$.

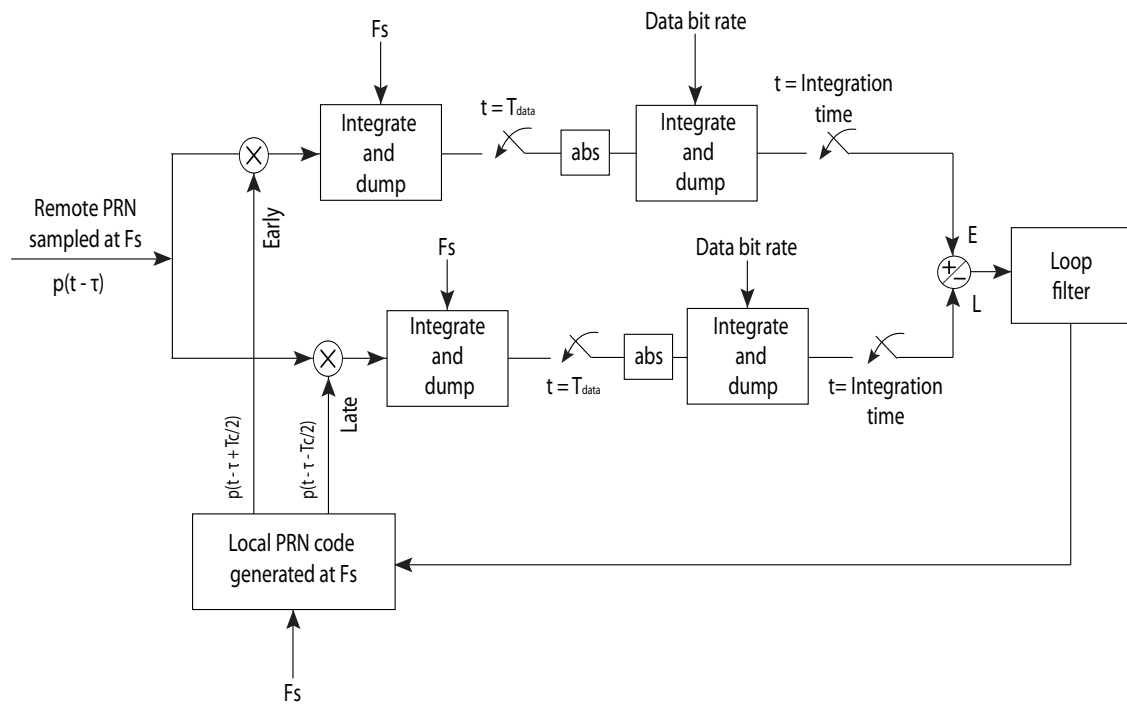


Figure 32: General schematic of the tracking architecture of DLL implementation.

4.2.4 Ranging Accuracy Limitations

The DLL scheme shown in Figure 32 was implemented in a C-simulation in order to study the influence of different noise sources and design parameters in the final ranging accuracy for LISA. The effects under investigation are:

1. Shot noise and limited phasemeter accuracy.
2. Presence of data encoded with a period shorter than a PRN sequence. (e.g. PRN length $\frac{1024}{F_c} = 655 \mu s$ and $T_d = \frac{1}{F_d} = 10 \mu s$).
3. Presence of a second PRN sequence.
4. Integration time.

Current results show that the system is capable of acquisition and tracking of the delay in the presence of these noise sources. The obtained instantaneous ranging precision in the order of 3 to 4 meters appears to be limited by the combination of data encoding and the presence of a second PRN sequence. The current implementation delivers measurements at kilohertz data rate, whereas TDI requires them at hertz rate, so that the resulting low rate ranging accuracy can be improved by post-processing.

Table 10 summarizes the ranging accuracy obtained after simulation with combinations of the three different noise sources and two possible integration times. Note that the ranging accuracy is limited by the presence of data when the integration time is a full PRN length. If a shorter integration time is implemented, the ranging accuracy is limited by the presence of a second PRN encoded in the input signal.

Shot noise	Integration time	2nd PRN	Data	rms ranging noise	Measurement rate
$4 \frac{\mu\text{rad}}{\sqrt{\text{Hz}}}$	1024	No	No	0.11 meters	1.5 kHz
$4 \frac{\mu\text{rad}}{\sqrt{\text{Hz}}}$	1024	Yes	No	0.39 meters	1.5 kHz
$4 \frac{\mu\text{rad}}{\sqrt{\text{Hz}}}$	1024	No	Yes	2.68 meters	1.5 kHz
$56 \frac{\mu\text{rad}}{\sqrt{\text{Hz}}}$	1024	Yes	Yes	3.48 meters	1.5 kHz
$56 \frac{\mu\text{rad}}{\sqrt{\text{Hz}}}$	256	No	No	2.95 meters	6 kHz
$56 \frac{\mu\text{rad}}{\sqrt{\text{Hz}}}$	256	Yes	No	5.21 meters	6 kHz
$56 \frac{\mu\text{rad}}{\sqrt{\text{Hz}}}$	256	No	Yes	4,27 meters	6 kHz
$56 \frac{\mu\text{rad}}{\sqrt{\text{Hz}}}$	256	Yes	Yes	5.78 meters	6 kHz

Table 10: Preliminary result of the ranging accuracy for combinations of three noise sources and two possible integration times

Future investigations will include simulations with time-varying delays, accuracy estimations after longer integration times and the hardware implementation of the presented design with optical signals.

4.2.5 Performance Improvement Options

These preliminary results support ranging accuracy of several meters. One of the dominant errors is contamination by the local (outgoing) PRN code imposed on the local oscillator. It is predicted that this error can be removed by also tracking the outgoing code, determining the cross correlation between the two codes, then subtracting this deterministic error from the measurement. The tracking of the second code would require an extra DLL channel in the phasemeter. Solving for the cross correlation and correcting the error could be performed on the ground. We estimate that a tenfold reduction in this error should be achievable.

Another limitation to ranging accuracy is the presence of data on the PRN code. A similar correction scheme may be employed to reduce this error. However, it may be simpler to turn off data encoding for a few seconds whenever an accurate ranging measurement is needed. Simulations are ongoing to investigate these issues.

4.3 Algorithm Errors

The displacement sensitivity of an interferometer with a single arm of length L is limited by fluctuations in the laser frequency ν by,

$$\frac{\tilde{L}}{L} \approx \frac{\tilde{\nu}}{\nu} \quad (47)$$

For an interferometer where two arms are differenced (e.g. a Michelson), we can replace the arm length L by the arm length mismatch ΔL in Eq. 47. As mentioned above, TDI effectively synthesizes a two arm interferometer configuration with (near) equal length arms. First generation TDI provides an equal arm length in the presence of a static arm length mismatch. However, the original TDI combinations will not in general produce equal arm interferometers in the presence of spacecraft relative motion [38]. Although each beam of the virtual two arm interferometer samples all interferometer lengths, they do so at slightly different times. Second Generation TDI corrects for velocity mismatch by sampling all the lengths a second time but with reversed order. This resampling averages out errors due to constant spacecraft velocity, leaving arm length errors due to acceleration mismatches and higher order derivatives. For the predicted LISA orbits it is expected that the Second Generation TDI combinations have equal length arms to better than 1 cm. Extrapolating from the results of Section 4.1 we estimate a maximum suppression factor of order $2 \times 10^9 \times (1 \text{ Hz}/f)$.

4.3.1 Performance Improvement Options

The arm length mismatch due to the acceleration of the spacecraft is negligibly small compared to the expected ranging errors. However if needed, acceleration correcting TDI combinations could be used. The main penalty associated with these algorithms is doubling of the start-up time needed to ensure that data is available with the appropriate delays (up to $16 \times L/C$ for the Michelson combinations).

4.4 Interpolation

TDI requires the phase measurements to be combined with precise delays. The phase measurements are made at a constant rate triggered by a local clock. Although the phasemeter samples the photodetector output at 50 MS/s the phase measurements are decimated to the relatively low sample rate of approximately 3 S/s. Phase measurements are made available at intermediate times by interpolating between samples [39]. Error in this interpolation process will limit the suppression of laser frequency noise by TDI.

Interpolation is achieved through fractional delay filtering. The interpolation error is determined by the frequency response of the digital filter. The filter kernel (impulse response) is typically a sinc function multiplied by a window to minimise spectral leakage. A longer filter kernel allows for more accurate interpolation at the expense of data loss at the beginning and end of a science run. Figure 33 shows the interpolation error as a function of kernel length for a range of filter kernel windows.

Increasing the phase measurement sampling rate significantly improves performance for a given kernel duration as it allows for a larger filter transition band. The trade-off between sample rate and kernel length are explored in [40]; there it was shown that sampling a band-limited signal at 3 Hz is acceptable for LISA assuming a laser frequency noise of $30 \text{ Hz}/\sqrt{\text{Hz}}$. Below we consider further improving the interpolation performance to accommodate free-running laser noise. We assume the free-running laser has a noise spectrum of

$$\tilde{\nu}_L = 10 \text{ kHz}/\sqrt{\text{Hz}} \times \frac{1 \text{ Hz}}{f} \quad (48)$$

which corresponds to a phase noise in the phase measurements of:

$$\tilde{\phi}_L = 2 \frac{\tilde{\nu}_L}{2\pi f^2} \quad (49)$$

$$\simeq 3.2 \times 10^3 \text{ cycles}/\sqrt{\text{Hz}} \times \left(\frac{1 \text{ Hz}}{f} \right)^2 \quad (50)$$

The factor of 2 in the numerator accounts for the transfer function of an arm peaking at 2 with phase-locked lasers. If the requirement for the measurement of phase is $\tilde{\phi}_M = 10^{-6} \text{ cycles}/\sqrt{\text{Hz}}$. The maximum allowable fractional error added by interpolation is then:

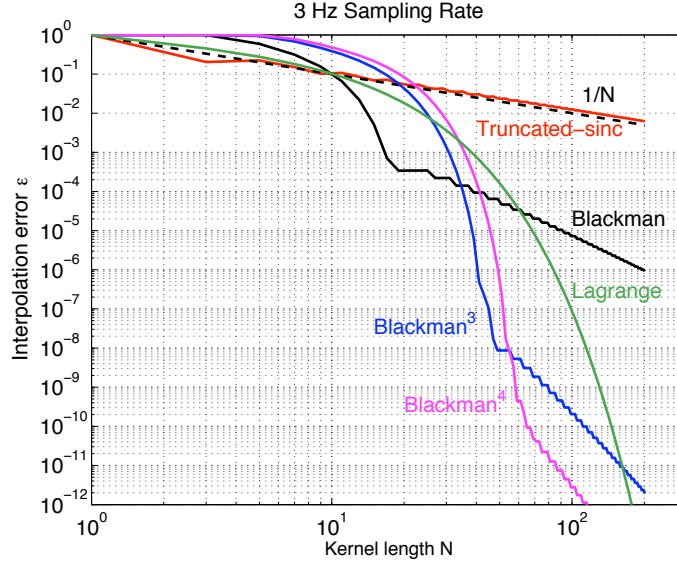


Figure 33: A comparison of interpolation error versus kernel length for windowed-sinc functions with different window.

$$\epsilon = \frac{\tilde{\phi}_M}{\tilde{\phi}_L} = 3.1 \times 10^{-10} \times \left(\frac{f}{1 \text{ Hz}} \right)^2 \quad (51)$$

This fractional error is plotted in Figure 34. Also shown in Figure 34, is the interpolation error from a filter with a 63 point kernel using a Blackman⁴ window and 3 S/s sampling rate. Note that the laser frequency noise increases at low frequencies but the interpolation error improves faster, so the 1 Hz error drives the filter design. With this kernel, 21 s of data is unusable at the start and end of each segment. This dead time could be decreased by increasing the sampling rate if desired.

The frequency noise suppression factor can be found by inverting equation 51 to give $3.2 \times 10^9 \times (1 \text{ Hz}/f)^2$.

4.4.1 Testbed Results Using Interpolation

The LISA Interferometry Testbed at JPL [29] uses interpolation to time shift the phase measurements before combining them into the TDI combination α . The testbed has two optical benches on which phase measurements are made with respect to two independent clocks. The relative drift of the clocks introduces an offset to the sample times of the phase measurement made at each bench. This offset is corrected by using interpolation to resample the measurements at the required times. Figure 35 shows that the dominant time

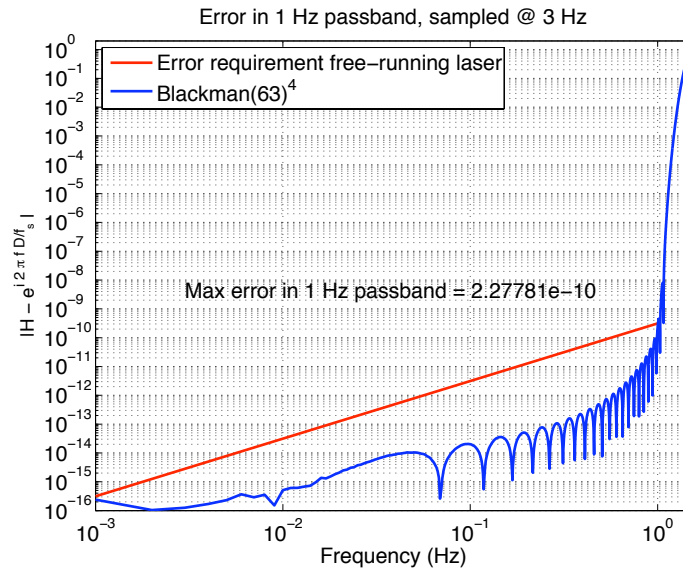


Figure 34: Error in the interpolation filter assuming a free-running laser of $10 \text{ kHz}/f\sqrt{\text{Hz}}$. A 63 point (21 seconds) Blackman⁴ filter achieves the required error.

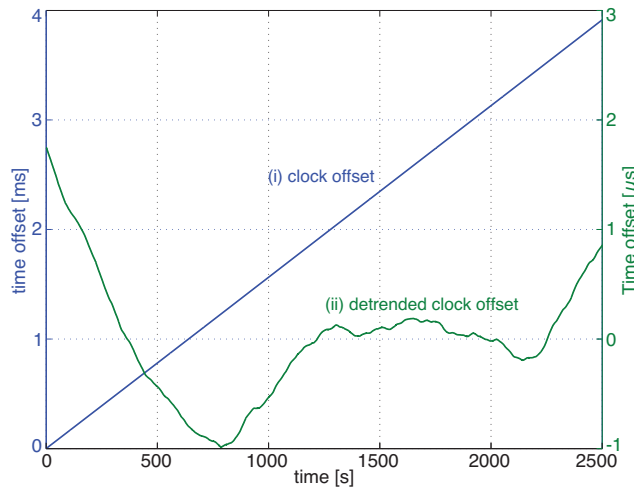


Figure 35: (i) Relative clock offset and (ii) detrended relative clock offset in the JPL LISA Interferometry Testbed. These offsets were inferred from optical transfer of clock noise, i.e. the sideband-sideband beat notes of 8 GHz phase modulation sidebands. In LISA the clock offsets will be extracted from the ranging measurements.

offset is a linear drift arising from a frequency offset of the two clocks. However, the μs level random clock fluctuations must also be accounted for when determining the correct time shift.

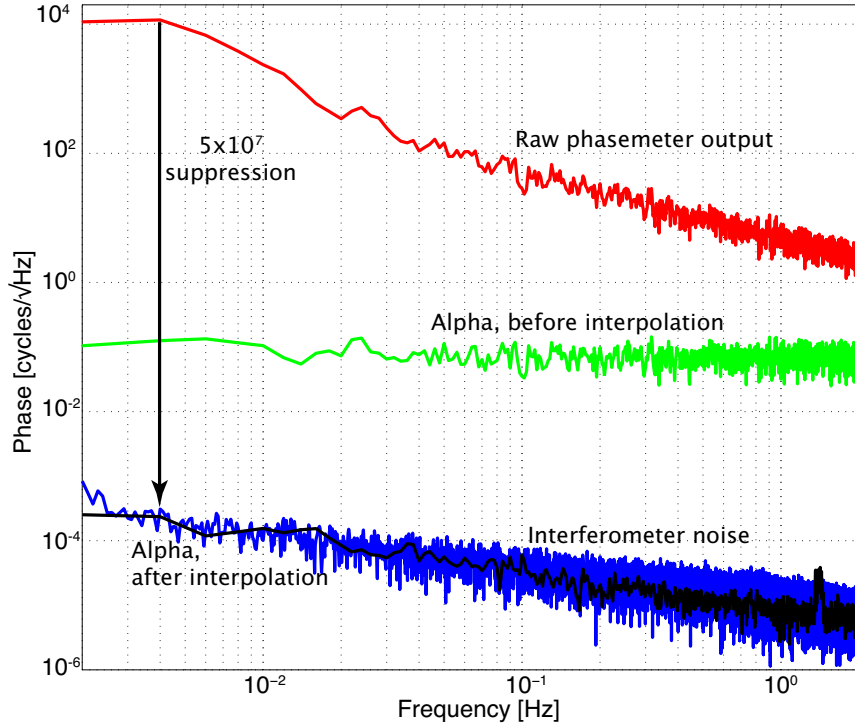


Figure 36: Experimental results from JPL LISA testbed with two independent spacecraft and clocks. The measured difference between the two clocks is shown in Figure 35.

Figure 36 shows the root power spectral density (RPSD) of the phase at different points in the signal processing chain. The upper trace shows the laser phase noise in a single phase measurement (raw phasemeter output). Each phase measurement contains approximately $30 \text{ Hz}\sqrt{\text{Hz}}$ of relative frequency noise imposed by intentionally adding noise to phase-locking. If the phase measurements are combined to form the α combination without interpolation then the laser frequency noise is only partially cancelled (labeled “alpha, before interpolation”). In this plot, the phase error due clock noise has been subtracted by incorporating the sideband-sideband beat note phase measurements into α . What remains is the residual laser noise due to incorrect delays. The bottom trace shows the noise in α after time shifting the phase measurements using interpolation. The laser frequency noise is suppressed by more than seven orders of magnitude at 3 mHz. In this test, the observable suppression was limited by the noise floor of the testbed.

4.4.2 Performance Improvement Options

The interpolation error vanishes quickly as the kernel length is increased. The cost is a longer dead time at the beginning and end of each science run. Increasing the (over)sampling rate also helps to substantially reduce the interpolation error at the cost of increased data rate to ground. It may be possible to have the best of both worlds by using a short kernel and fast sample rate at the beginning (and end) of a run to reduce dead time, then reverting to a longer kernel and lower sampling rate to save on data costs for the majority of science operations. There is little motivation to move to this more complicated approach given the currently estimated performance of interpolation.

It is possible that the current formulation of interpolation requirements is overly conservative. In particular, it may be permissible to place a requirement only on the difference of the transfer functions of any two phasemeters, rather than on the transfer function itself. The transfer functions will be very closely matched as the filters are implemented digitally using identical kernels. The transfer functions will vary because of the different sampling rates used by the clock's on each spacecraft. As the more conservative requirement can be met fairly easily with little or no impact on flight hardware design we have deferred further examination of this issues.

4.5 Analog Chain

We consider the sensitivity to laser frequency noise of the analog electronics chain, which consists of a photoreceiver, adjustable-gain preamplifier, and anti-alias filter (Figure 37). To evaluate the performance of the subsystem, phase error at the output of the chain is

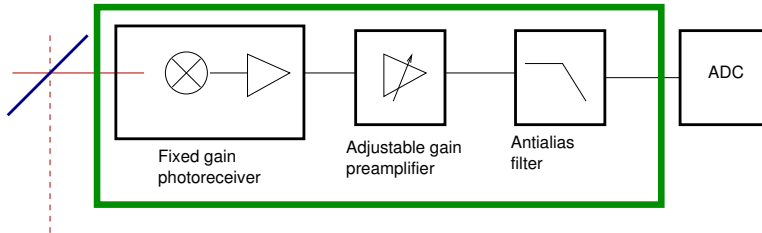


Figure 37: The analog electronics chain is within the green box. The input of the chain is a light beam from the beamsplitter, and the output is the electrical voltage delivered to the ADC.

estimated in the presence of frequency noise in the input optical beam. Two mechanisms relating analog electronics to frequency noise are considered: dispersion, a phase delay effect that can degrade the accuracy of ranging needed for TDI, and nonlinearity (“fidelity error”). We do **not** consider here noise terms that are associated with analog electronics that are unrelated to frequency noise, including electronic noise at the heterodyne frequency (NEP);

phase noise at the gravitational wave signal frequency (including temperature sensitivity of cables); suppression of timing ADC phase noise by pilot tone; suppression of intensity noise at heterodyne frequency by subtraction of anti-phased beamsplitter outputs.

4.5.1 Key Parameters and Assumptions

Phase slope and range error

The analog electronics chain introduces a group delay τ_e between the input light and the output signal. The group delay is related to the phase by $\tau_e = d\Phi/df$. Here $\Phi(f)$ (in units of cycles) has the conventional meaning of phase difference between input and output of the electronics chain; we are concerned with the response near the heterodyne signal frequency, $2 \text{ MHz} < f_h < 18 \text{ MHz}$. Group delay is a mechanism for converting frequency noise $\tilde{\nu}(f_s)$ in the signal band, $f_s < 1 \text{ Hz}$, to phase noise in the signal band: $\tilde{\Phi}(f_s) = \tau_e \tilde{\nu}(f_s)$. This conversion appears to place a tight constraint on the allowed group delay for a given level of frequency noise. For example, requiring $\tilde{\Phi}(f_s)$ from group delay to be $< 1 \mu\text{cycle}/\sqrt{\text{Hz}}$ in the presence of $\tilde{\nu}(f_s) = 300 \text{ Hz}/\sqrt{\text{Hz}}$ would seem to require $\tau_e < 3 \text{ ns}$ throughout the range of heterodyne frequencies, a demanding requirement. With some attention paid to the method used for measuring range, however, the allowed group delay can be relaxed by orders of magnitude.

The requirement on group delay is relaxed by arranging the range measurement to be common with the science phase measurement. The baseline plan calls for using the same electronics chain for ranging and science phase—that is, the electronics shown in Figure 37. If the science measurement is made at the same frequency as the range measurement, both see the same τ_e , and group delay introduces no error. The key determiner of error due to analog electronics delay is the sideband deviation of the ranging measurement.

Dispersion Dispersion is defined as the slope of the group delay vs. frequency curve: $D(f) = d\tau_e/df = d^2\Phi/df^2$. Limited bandwidth in the analog chain results in dispersion, which in turn results in $\tau(f_1) \neq \tau(f_2)$, where f_1 and f_2 are the frequencies used for ranging and science measurements. For example, model the chain as n cascaded simple low-pass filters, each of characteristic frequency f_0 . The transfer function of this model is

$$T(f) = \left(\frac{1}{1 + if/f_0} \right)^n. \quad (52)$$

This transfer function has group delay of

$$\tau(f) = \frac{n}{2\pi} \frac{f_0}{f_0^2 + f^2}. \quad (53)$$

As a conservative extreme, assume low-bandwidth electronics: $n = 3$, $f = 20 \text{ MHz}$, (worst-case heterodyne frequency), $f_0 = 40 \text{ MHz}$ (minimum acceptable bandwidth). The value of Δf , the frequency difference between range and science phase measurements, depends on the ranging method. In the baseline method, pseudo-random sidebands are

imposed, with sideband deviation $\Delta f = 1$ MHz. If the sidebands are unbalanced or if only one of the upper and lower sidebands is used for ranging, the resulting range error is

$$\Delta\tau_e = \frac{d\tau}{df} \Delta f = 191 \text{ ps}, \quad \epsilon_r = 6 \text{ cm.} \quad (54)$$

The baseline plan has balanced sidebands for ranging, in which case

$$\Delta\tau_e = \frac{1}{2} \frac{d^2\tau}{df^2} (\Delta f)^2 = 1.0 \text{ ps}, \quad \epsilon_r = 0.3 \text{ mm.} \quad (55)$$

If implicit ranging [41] with 1 Hz tone is used instead of the baseline design, then $\Delta f = 1$ Hz, and ϵ_r due to dispersion would be 60 nm, negligible by several orders of magnitude compared to other limitations to ranging such as signal-to-noise ratio.

Nonlinearity Nonlinear effects in analog electronics, or fidelity errors, are difficult to characterize analytically and are best measured experimentally. As an extreme test, the single-bench interferometer testbed at JPL was operated with free-running lasers (Figure 38). The testbed was originally designed to have the slave laser phase-locked to the

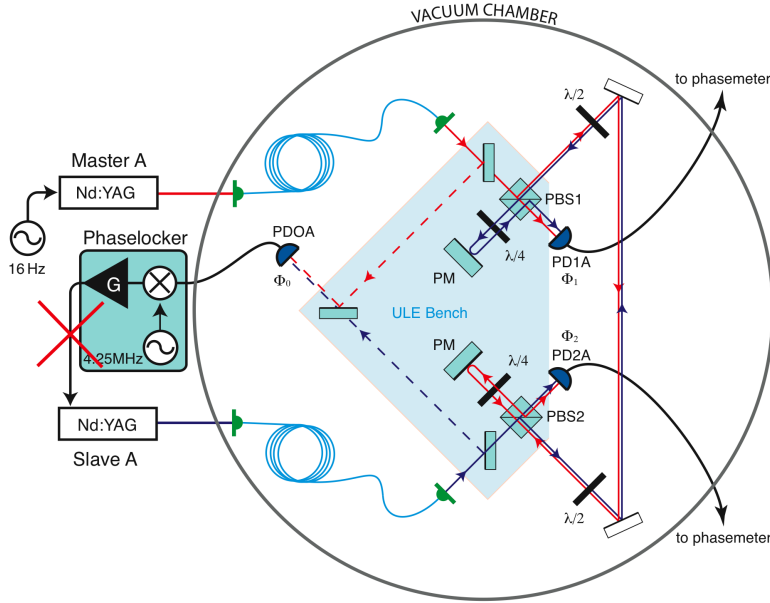


Figure 38: Single bench testbed. The feedback to the lower laser is broken, leaving both lasers free-running.

master laser via the “back link” interferometer. For the nonlinearity test, the feedback to

the nominal slave laser was disconnected, leaving both lasers free-running and independent of one another. As a result, the individual Sagnac signals, Φ_1 and Φ_2 were very large; as shown in Figure 39, $\Phi_{1,2}(f_s) \approx 5 \times 10^3 \text{ cycles}/\sqrt{\text{Hz}} \times (1 \text{ Hz}/f)^2$. After time-shifting to form

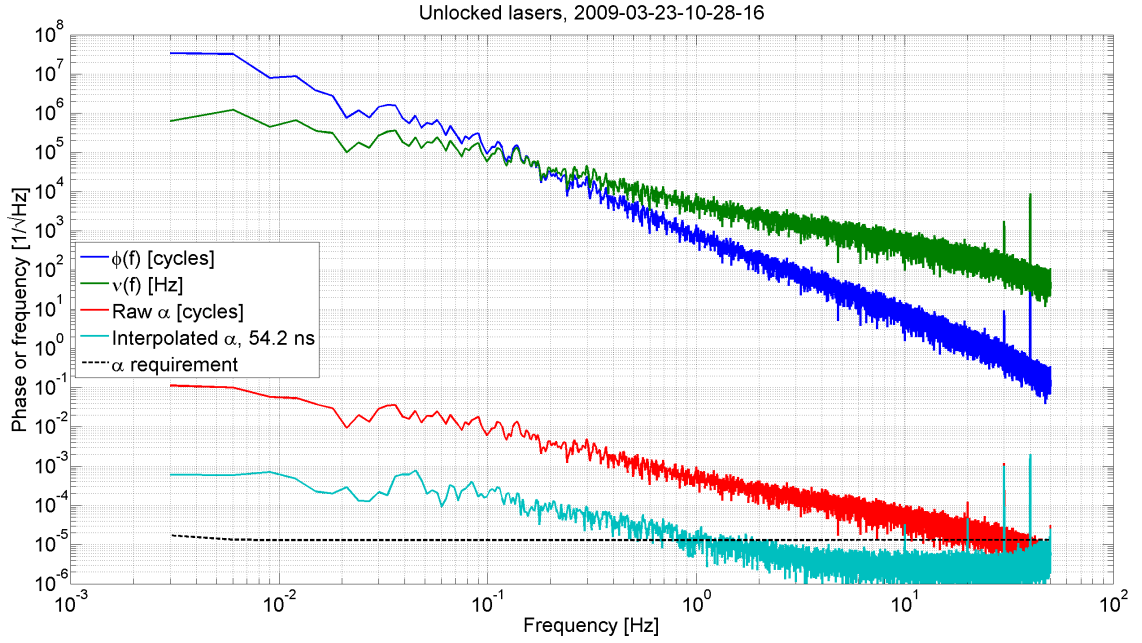


Figure 39: Noise of various signals in single-bench experiment with unlocked lasers.

the α TDI combination, the noise level is suppressed by approximately $5 \times 10^7 \times (1 \text{ Hz}/f)$.

4.5.2 Reference Performance

Figure 40 shows a transfer-function measurement of a prototype quadrant photoreceiver. The overall variation in phase (Φ [deg]) is a result of the limited bandwidth of the front-end electronics. The total variation in τ_e is less than 7 ns, and the maximum variation over 1 MHz is $\Delta\tau = 3$ ns. This is much larger than the model estimates of Section 4.5.1, and is believed to arise from fluctuations in the measurement of reference phase, derived from an independent photoreceiver. As a measurement upper limit, the worst-case ranging method—1 MHz, unbalanced ranging sidebands—would introduce the same sensitivity to frequency noise as a ranging error of 1 m.

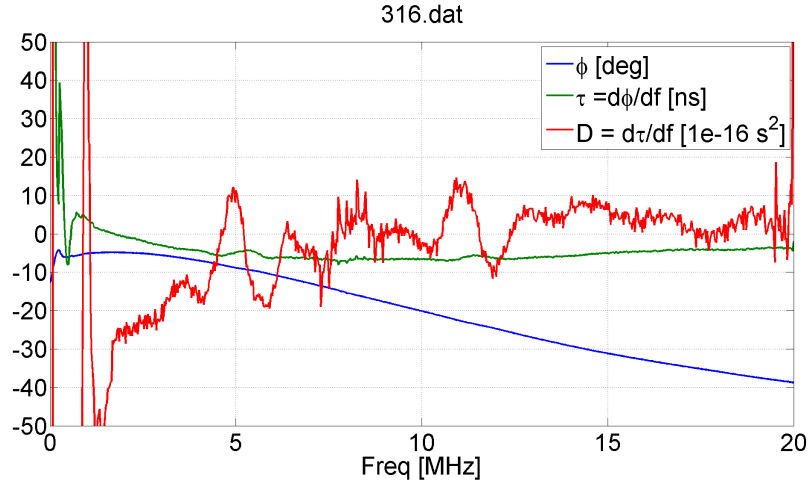


Figure 40: Measurement of phase response $\Phi(f)$, and corresponding group delay $\tau = d\Phi/df$ and dispersion $D = d\tau/df$, for frequencies spanning the range of LISA heterodyne frequencies.

4.5.3 Performance Improvement Options

Design and testing of photoreceivers will continue, with the objective of demonstrating the expected lower level of dispersion. Concurrently, the implicit ranging technique will be investigated as a method that makes the LISA science measurement almost completely insensitive to dispersion.

4.6 Phasemeter Digital Signal Processing

Non-linearity of the phasemeter digital signal processing can limit the suppression factor of TDI. A measurement of the TRL 4 phasemeter's linearity was made by measuring three digital data streams representing beatnotes between three independent lasers. This linearity test is actually a test of the superposition principle, commonly stated as $f(a) + f(b) = f(a + b)$. For our purposes a , b and $(a + b)$ are the true phases of the heterodyne signals and $f(x)$ is the result of the phase measurement of heterodyne signal with phase x . In our case, we use a slightly modified superposition:

$$f(a - b) + f(b - c) - f(a - c) = 0 \quad (56)$$

This relationship is symmetric in the sense that each of the three terms has the same RMS noise level (assuming a , b , and c do also). The measurement also more closely simulates the LISA arrangement, where each heterodyne signal phase is the difference of two laser phases. The equivalent optical setup is shown in Figure 41.

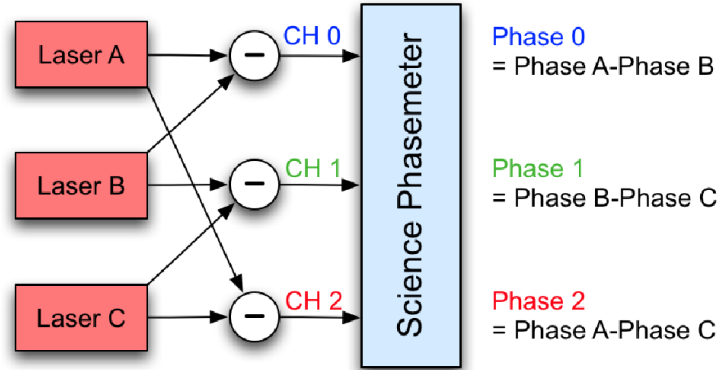


Figure 41: Block diagram of equivalent optical set up for digital tests of phasemeter linearity.

The test was conducted using a digital signal generator, implemented on a separate FPGA. The digital signal generator generates three signals with phase correlations satisfying equation 56 to isolate the non-linearity of the digital signal processing. The individual heterodyne signals' phase noise spectra were approximately $10^4 \text{ cycles}/\sqrt{\text{Hz}} \times (1 \text{ Hz}/f)^2$. Each phase measurement produced what appears to be uncorrelated, random noise. When the three phase difference outputs are combined appropriately, the noise should add to zero; any residual noise is attributed to non-linearity in the phasemeter. Figure 42 shows that the residual noise root power spectral density of the 3 channel sum is $2 \mu\text{cycle}/\sqrt{\text{Hz}}$ (limited by the known, internal quantization noise of the breadboard phasemeter). This test demonstrates that the phasemeter DSP does not limit the TDI suppression factor at the level of $10^{10} \times (1 \text{ Hz}/f^2)$.

4.7 Scattered Light

Scattered light is another source of frequency noise induced non-linearity. We consider light from a particular interferometer beam leaving that beam, travelling some different optical path, and then rejoining that same beam. The stray or scattered beam must end up well aligned with the main beam if it is to have any effect on the interferometric measurement. To determine the effect of this scattered light on the LISA phase measurements we start by considering an optical beam of amplitude 1. To this beam we add a small amount of extra light of amplitude a ($a \ll 1$) as shown in the phasor diagram of Figure 43.

This light is of the same frequency as the original beam but has travelled a different distance, so that its phase with respect to the original beam is ϕ_s . We can then calculate

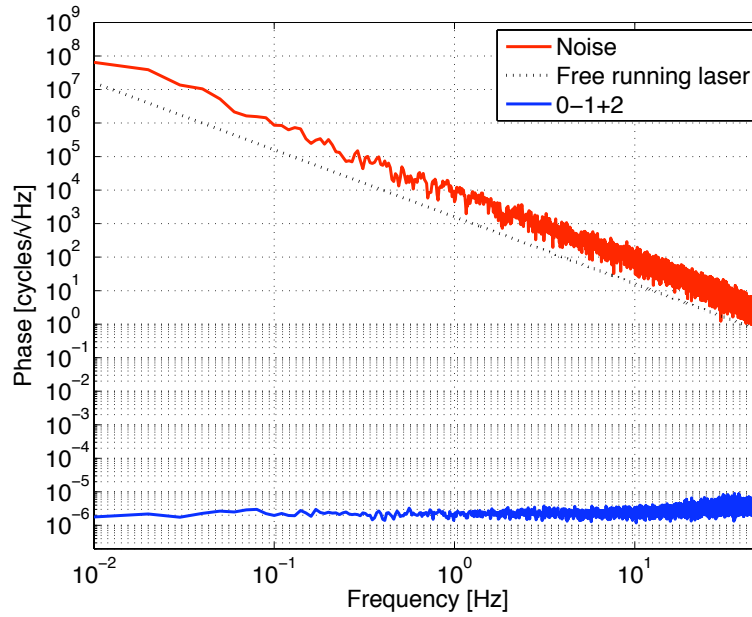


Figure 42: Phasemeter DSP linearity test using three correlated noise sources.

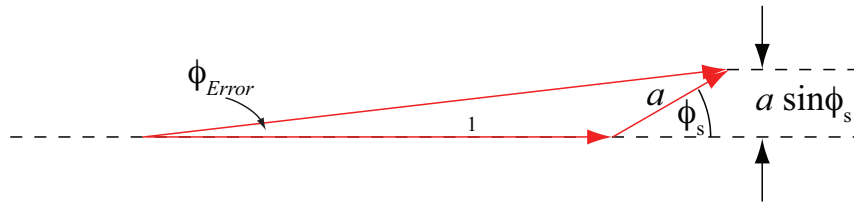


Figure 43: Phasor diagram illustrating the phase error caused by scattered light.

the phase error this will introduce to the original beam as:

$$\phi_{Error} = a \sin \phi_s \quad (57)$$

or equivalently

$$x_{Error} = \frac{a\lambda}{2\pi} \sin \phi_s \quad [\text{m}/\sqrt{\text{Hz}}] \quad (58)$$

If the phase of the scattered light is varying with time then this will produce a time varying phase, or displacement, error as calculated below.

The relative phase of scattered light depends on the laser frequency and the extra path length of the scattered light d .

$$\phi_s = 2\pi\nu d/c \quad [\text{rad}] \quad (59)$$

The phase change of the scattered light is,

$$\Delta\phi_s = \frac{\partial\phi_s}{\partial\nu}\Delta\nu + \frac{\partial\phi_s}{\partial d}\Delta d \quad (60)$$

The first term is the phase change due to laser frequency changes and the second term is the phase change due to changes in path length to the scattering source. In the context of laser frequency noise cancellation we are interested only in the first term and the second term is neglected for the remainder of this analysis; for a complete treatment of both terms see [42]. From Eq. 59 we can see,

$$\frac{\partial\phi_s}{\partial\nu} = 2\pi d/c \quad \left[\frac{\text{rad}}{\text{Hz}} \right] \quad (61)$$

and so,

$$\Delta\phi_s = \frac{2\pi d}{c}\Delta\nu \quad [\text{rad}] \quad (62)$$

For scattered light that has traveled an extra path length of d then, even if this length is stable, a change of laser frequency will change the relative phase of the main and scattered light beams.

We can consider two cases (i) the change in ϕ_s is small ($\ll 1$) and (ii) the change in ϕ_s is large compared to a cycle ($\gg 1$).

Case 1: For $\Delta\phi_s \ll 1$ we can approximate Eq. 57 to,

$$\begin{aligned} \phi_{Error} &\approx a\phi_s \\ \Delta\phi_{Error} &\approx 2\pi\frac{ad}{c}\Delta\nu \end{aligned} \quad (63)$$

This small angle approximation gives the worst case phase error due to scattered light (the slope of sine is maximum at zero). For a stationary scattering point, this assumption implies that $\Delta\nu \ll 2\pi c/d$ (e.g. $\Delta\nu \ll 300$ MHz for $d = 1$ m). This is a good approximation for Fourier frequencies in the LISA band (even the free-running laser noise is expected to be ≈ 10 MHz/ $\sqrt{\text{Hz}}$ at 1 mHz).

The limit to the suppression factor due to scattered light can be found by converting the laser frequency noise phase noise $\Delta\phi_\nu = \Delta\nu/f$ [rad].

$$\frac{\Delta\phi_\nu}{\Delta\phi_{Error}} \sim \frac{c}{adf} \quad (64)$$

Using pessimistic estimates of scattered light [42] we assume the $a < 2e - 5$ and $d = 1$ m we arrive at a suppression factor $1.5 \times 10^{13} \times (1 \text{ Hz}/f)$.

Case 2: At frequencies well below the LISA band the laser frequency drift could be significantly larger and we could expect $\Delta\phi_s \gg 1$. Long term drift of the laser frequency coupled with the periodic nonlinearity of the scattering error (Eq. 57) will upconvert low frequency laser noise to produce an error at frequencies within the LISA band. To avoid this, we should ensure that the laser does not drift through one scattering “fringe” faster than say, 10,000 seconds. The scattered fringe is c/d Hz. so we must ensure that $\delta(\Delta\nu)/\delta t < c/d/10^4$ or a frequency drift of less than 300 kHz/s. This leaves substantial margin over the worst case frequency drift caused by Doppler knowledge error and arm locking of around 5 kHz/s (assuming a 600 kHz common arm Doppler knowledge error).

4.8 Summary

Comparing all known effects it is apparent that errors in the ranging/timing limits the TDI frequency noise suppression. With 1 m ranging and 1 pm allocation a laser frequency noise 141 Hz/rt(Hz) could be tolerated.

Part II

Frequency Noise Suppression System Options

This section describes how the individual frequency noise suppression techniques are combined into systems capable of meeting LISA’s frequency noise requirement. We consider four combinations of techniques listed in Table 11.

Table 11: Summary of system options performance. The margin for systems including arm locking depends on the arm length mismatch. Values for margin assume a Time-Delay Interferometry performance limited by 1 m ranging error.

Suppression System	Margin at 3 mHz		Margin at 1 Hz	
	$\Delta\tau = 0.51$ s	$\Delta\tau = 0.026$ s	$\Delta\tau = 0.51$ s	$\Delta\tau = 0.026$ s
Fixed cavity	10		10	
Arm locking only	5	5	1.8	2.4
Cavity & arm locking	16000	800	1500	2000
Mach-Zehnder & arm locking	13000	800	54	75

In all options, one laser is designated as the master laser and all other active lasers in the constellation are phase-locked to the master with appropriate frequency offsets. The residual phase-locking error is assumed to be negligible compared to the laser phase noise after stabilization. The lasers are assumed to have a free-running frequency noise characterized by a linear spectral density of approximately,

$$\Delta\nu = 30 \text{ kHz}/\sqrt{\text{Hz}} \cdot \left(\frac{1 \text{ Hz}}{f} \right) \quad (65)$$

TDI is common to all designs. The allocated equivalent single-link path length noise to residual laser frequency noise (post-TDI) is assumed to be $2 \text{ pm}/\sqrt{\text{Hz}} \cdot \sqrt{1 + (3 \text{ mHz}/f)^4}$, the value in the Requirements Flowdown Document. This allocation is converted to a pre-TDI frequency noise allocation using Eq. 42 (Section 4), which assumes that the TDI suppression factor is dominated by 1 m ranging errors. This allocation implies a laser frequency noise stability allocation described by,

$$\nu_{stab} = 282 \text{ Hz}/\sqrt{\text{Hz}} \cdot \left[\frac{1 \text{ m}}{\Delta L} \right] \cdot \sqrt{1 + (3 \text{ mHz}f)^4}. \quad (66)$$

For options using arm locking, we assume that modified dual arm locking is used, as described in section 3.3.

5 Fixed Cavity

The master laser is locked to a fixed Fabry-Perot cavity of moderate finesse using the Pound-Drever-Hall (PDH) technique. One option for the optical and electronic interfaces between the relevant subsystems are shown in Figure 44.

5.1 Design Summary

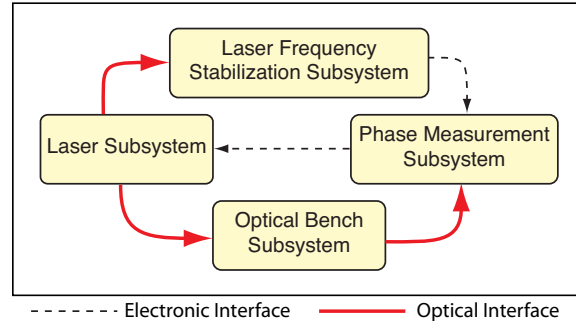


Figure 44: Subsystem interface diagram for Fixed Cavity Stabilization

The optical interface between the Laser Subsystem and the Frequency Stabilization Subsystem is unmodulated light delivered by an optical fiber. The PDH sidebands are imposed by a phase modulator contained within the laser frequency stabilization subsystem. The Frequency Stabilization Subsystem contains a waveguide modulator, optical cavity and photoreceiver. In this diagram it is assumed that the Phase Measurement Subsystem implements the demodulation of the PDH error signal and feedback controller, however this functionality could instead be included in the Frequency Stabilization Subsystem. The electrical interface between the Frequency Stabilization Subsystem and the Phase Measurement Subsystem is an analog electronic signal from the PDH photoreceiver. The laser frequency control operates in two distinct modes: pre-stabilization and phase-locking. Only one mode is active at any time and there is no interaction between these control loops. Not shown is the frequency distribution subsystem and its interfaces with the Laser Frequency Subsystem, the Phase Measurement Subsystem and the Laser Subsystem.

The cavity's control system parameters are summarized in Table 12. The noise floor is set at a level that is consistent with measurements made in several laboratories. The unity gain frequency was chosen to be near the intersection of the cavity noise floor with the free-running laser noise to avoid adding noise at high frequencies. With a controller slope of $1/f$ or steeper, the open-loop gain is sufficient to reach the cavity noise floor at all frequencies below the unity gain frequency, making the exact details of the controller immaterial.

Table 12: Parameter summary for cavity stabilization

Parameter	Value
Cavity Noise Floor	$30 \text{ Hz}/\sqrt{\text{Hz}} \cdot \sqrt{1 + (3 \text{ mHz}/f)^4}$
Unity Gain Frequency	$\sim 1.8 \text{ kHz}$

5.2 Performance

The frequency noise of the cavity-stabilized laser is shown in Figure 45 compared to the free-running laser and the TDI capability for 1 m ranging. The frequency stability is determined by the noise floor of the cavity (sensing). This plot shows that with 1 m ranging accuracy, cavity stabilization would meet the frequency noise allocation with a margin of approximately 10 across the LISA signal band.

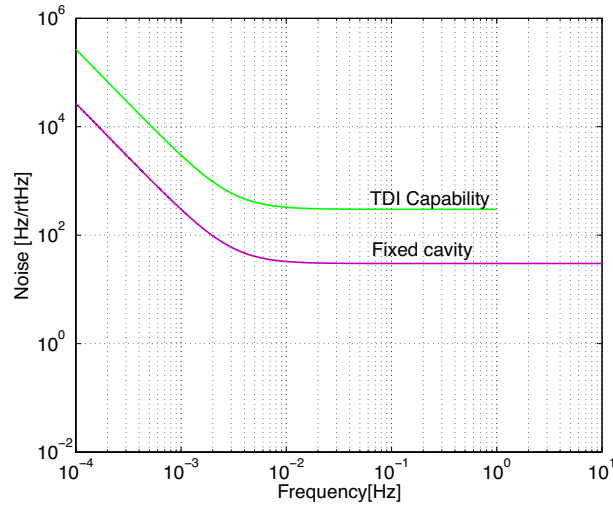


Figure 45: Frequency noise after cavity stabilization compared to the TDI capability (frequency noise requirement) assuming 1 m ranging accuracy.

6 Arm Locking Only

In this option the master laser is frequency stabilized using modified dual arm locking with no pre-stabilization.

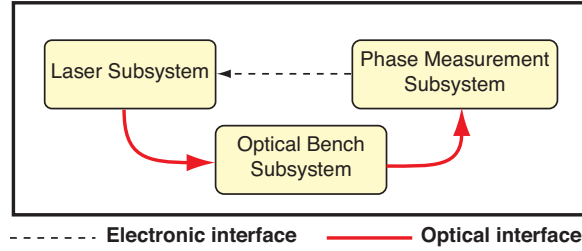


Figure 46: Subsystem interface diagram for Arm Locking only option.

6.1 Design Summary

A block diagram of the interfaces between key subsystems is shown in Figure 46. The laser frequency control operates in two distinct modes: phase-locking and arm locking. Not shown is the frequency distribution subsystem and its interfaces with the Phase Measurement Subsystem and the Laser Subsystem. The Optical Bench Subsystem in this option is unchanged from the Fixed Cavity case. In the Phase Measurement Subsystem the Fixed Cavity demodulation and frequency controller is removed and a modified dual arm locking controller is needed. The controller and sensor transfer function for modified dual arm locking is described in detail in Section 3.

Table 13: Summary of arm locking control system parameters.

Parameter	value
Sensor	Modified Dual Arm Locking [30]
gain @ 3 mHz	87,000
lower UGF	4.8 μ Hz
upper UGF	14.7 kHz

6.2 Performance

The frequency noise after arm locking is shown in Figure 47, along with the TDI capability assuming 1 m ranging accuracy. This design meets the requirements with the possible exception of the extreme low-end of the LISA band (less than 0.1 mHz). Note that this spectra was achieved assuming the worst case (minimum) arm-length difference, $\Delta\tau = 0.026$ s.

7 Arm Locking with Tunable Cavity Pre-stabilization

The master laser is stabilized to a fixed reference cavity with an adjustable frequency offset provided by offset sideband locking. The master laser is further stabilized by generating

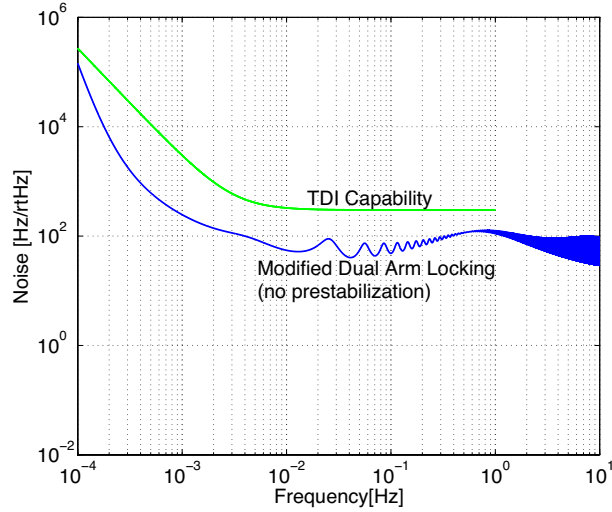


Figure 47: Laser frequency noise after stabilization by modified dual arm locking with no pre-stabilization. Arm length mismatch of $\Delta\tau = 0.026\text{s}$

an arm locking error signal, filtering it through a controller, and feeding it back to both the sideband offset and the laser frequency actuators.

7.1 Design Summary

The optical interface between the Laser Subsystem and the Frequency Stabilization Subsystem is unmodulated light delivered by an optical fiber. The sidebands are imposed by a phase modulator contained within the laser frequency stabilization subsystem. The signal used to drive the phase modulator must have an adjustable center frequency with a tuning range greater than approximately 10 MHz to accommodate the frequency pulling of arm locking. This sinusoidal signal is also phase modulated at a frequency of approximately 5 MHz to produce the PDH sidebands. The Frequency Stabilization Subsystem contains a waveguide modulator, optical cavity, photoreceiver and a voltage controlled oscillator (VCO) or numerically controlled oscillator (NCO) used to adjust the offset frequency for the sideband modulation. Once again it is assumed that the Phase Measurement Subsystem implements the demodulation of the PDH error signal and feedback controller, however this functionality could also be included in the Frequency Stabilization Subsystem. The electrical signal from the Frequency Stabilization Subsystem to the Phase Measurement Subsystem is an analog electronic signal from the PDH photoreceiver. The signal from the Phase Measurement Subsystem to the Frequency Stabilization Subsystem is a correction signal (analog or digital) to adjust the frequency of the VCO/NCO. The usual interfaces to the frequency distribution subsystem are not shown.

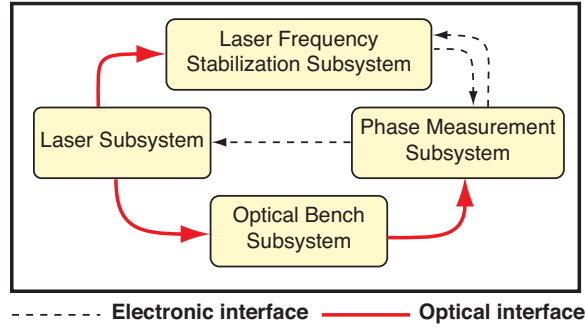


Figure 48: Subsystem interface diagram for Cavity and Arm Locking option.

Pre-stabilization with arm locking is nested control system. The performance of such a system depends on the details of how the signals are combined. As shown in Figure 49, the laser is pre-stabilized to the cavity. An additional error signal from arm locking is incorporated at two points. The arm locking feedback signal is used to adjust the frequency of the light entering the cavity (point A in Figure 49). This is achieved by changing the modulation frequency used to produce the resonant sideband. The arm locking feedback signal is also added to the PDH correction signal and fed back to the laser frequency actuator (point B in Figure 49). This second correction point allows the arm locking control system to be optimized independently of the bandwidth of the cavity stabilization control loop.

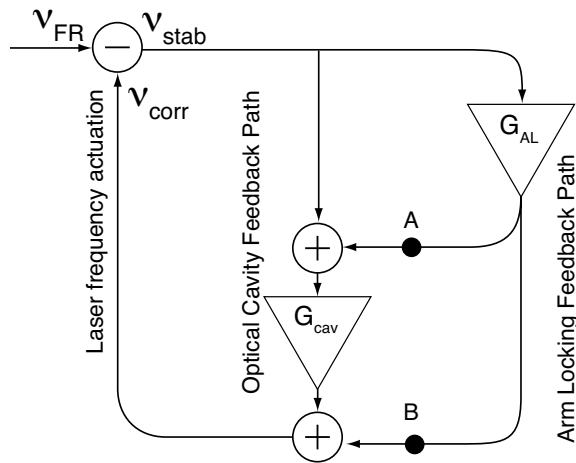


Figure 49: Nested feedback loops for arm locking with a fixed cavity

We can express the stabilized laser frequency ν_{stab} in terms of the free-running laser

frequency noise, ν_{FR} and the frequency correction ν_{corr} .

$$\nu_{stab} = \nu_{FR} - \nu_{corr} \quad (67)$$

ν_{corr} is made up of contributions from both the arm locking and PDH error signals.

$$\nu_{corr} = \nu_{stab} (G_{cav} + G_{AL}G_{cav} + G_{AL}) \quad (68)$$

where G_{cav} and G_{AL} are the total open loop gains of the cavity and arm locking control systems respectively. Rearranging to solve for the noise suppression we get,

$$\frac{\nu_{stab}}{\nu_{FR}} = \frac{1}{1 + G_{cav} + G_{AL}G_{cav} + G_{AL}} \quad (69)$$

$$= \left(\frac{1}{1 + G_{cav}} \right) \left(\frac{1}{1 + G_{AL}} \right) \quad (70)$$

From Equation 70 we can see that the total frequency noise suppression is the product of the noise suppression of the individual loops.

7.2 Performance

The frequency noise after cavity pre-stabilization and arm locking is shown in Figure 50. This design meets requirements for TDI 1 m ranging accuracy with a margin of greater than 800 across the LISA band. The hump in the noise floor near 3 mHz is due to clock noise coupling into the arm locking sensor and is only present for small arm-length differences.

8 Arm Locking with Mach-Zehnder Pre-stabilization

In this configuration the master laser is stabilized to a Mach-Zehnder interferometer as described in Section 2.5. The master laser is further stabilized by generating an arm locking error signal, filtering it through a controller, and feeding it back to offset the Mach-Zehnder lock point. This is achieved by adjusting the phase of the numerically oscillator used to demodulate the Mach-Zehnder heterodyne signal. The arm locking correction is also fed back to the laser frequency directly as discussed below.

8.1 Design Summary

The optical bench subsystem is modified to include the extra interference path needed to produce the arm length mismatched Mach-Zehnder. An extra channel is added to the Phase Measurement Subsystem to determine the phase of this heterodyne signal. As described in Section 2.5, the phase of this signal depends on the master laser frequency relative to the Mach-Zehnder arm length difference. The Phase Measurement Subsystem would also

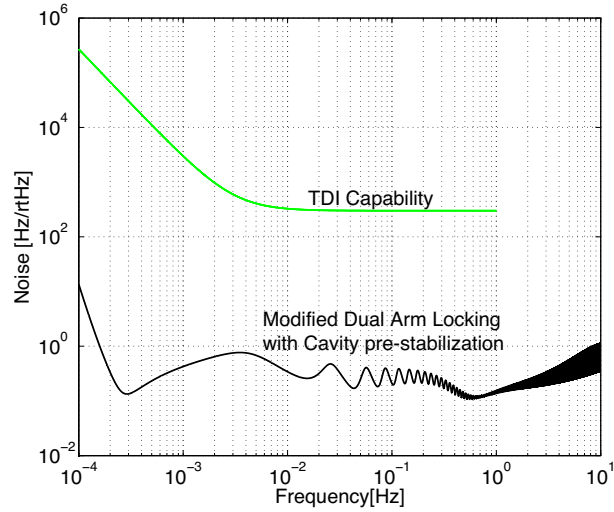


Figure 50: Laser frequency noise after stabilization by modified dual arm locking with cavity pre-stabilization. Arm length mismatch of $\Delta\tau = 0.026\text{s}$

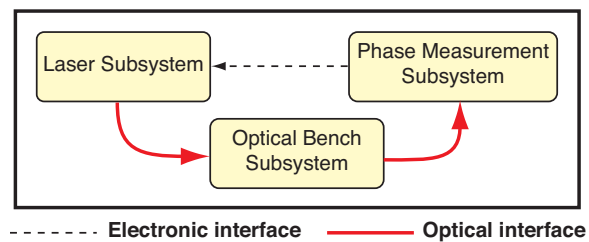


Figure 51: Subsystem interface diagram for Mach-Zehnder and Arm Locking option.

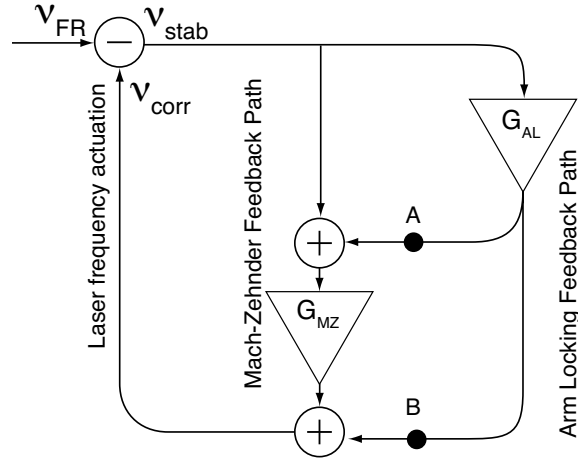


Figure 52: Nested feedback loops for arm locking with Mach-Zehnder stabilization

include a pre-stabilization controller, needing only minimal modifications from the usual phase-locking controller.

The Mach-Zehnder and arm locking stabilization systems are combined as shown in Figure 52. Following the derivation in the previous section, the closed loop noise suppression of laser frequency noise is given by,

$$\frac{\nu_{stab}}{\nu_{FR}} = \left(\frac{1}{1 + G_{MZ}} \right) \left(\frac{1}{1 + G_{AL}} \right). \quad (71)$$

If we include sensor noise in both the Mach-Zehnder and arm locking control loops, we arrive at the total closed loop frequency noise of,

$$\nu_{stab} = \frac{\nu_{FR}}{(1 + G_{MZ})(1 + G_{AL})} - \frac{N_{MZ}G_{MZ}}{(1 + G_{MZ})(1 + G_{AL})} - \frac{N_{AL}G_{AL}}{(1 + G_{AL})}. \quad (72)$$

This shows that the Mach-Zehnder closed-loop sensor noise, $N_{MZ}G_{MZ}/(1 + G_{MZ})$ is suppressed by the arm locking gain, $(1 + G_{AL})$. The arm locking sensor noise N_{AL} is directly imposed on the stabilized laser frequency.

The Mach-Zehnder frequency stabilization properties are summarized in Table 14. A path length difference of 50 cm is assumed for the frequency reference interferometer, which sets both the frequency discriminant and tuning coefficient for the loop. The error point noise, a combination of path length noise and phase measurement noise, is set at an equivalent path length noise of $1 \text{ pm}/\sqrt{\text{Hz}}$ with a roll-up below 2 mHz.

The arm locking controller is summarized in Table 7. With a unity gain frequency of 20 Hz, the Mach-Zehnder pre-stabilization should be readout noise limited at all frequencies in the LISA science band, yielding a level of $800 \text{ Hz}/\sqrt{\text{Hz}}$ prior to arm locking.

Table 14: Parameters assumed for Mach-Zehnder pre-stabilization

Parameter	Value
Path length difference	50 cm
Error point noise	$(1 \mu\text{cycle}/\sqrt{\text{Hz}}) \cdot \sqrt{1 + (2 \text{ mHz}/f)^4}$
Unity Gain Frequency	$\sim 20 \text{ Hz}$

8.2 Performance

Figure 53 shows the frequency noise after Mach-Zehnder pre-stabilization and arm locking. This design meets requirements with a margin greater than 50 at 1 Hz and 800 at 3 mHz. The hump in the arm locking noise floor near 4 mHz is due to clock noise coupling into the arm locking sensor and is only present for small arm-length differences.

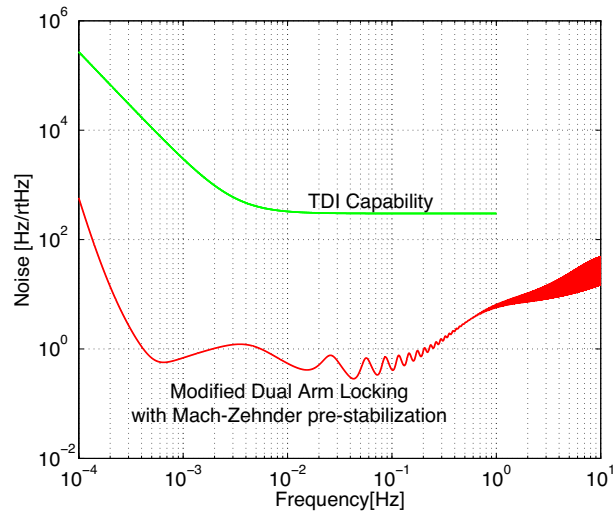


Figure 53: Laser frequency noise after stabilization by modified dual arm locking with Mach-Zehnder pre-stabilization. Arm length mismatch of $\Delta\tau = 0.026\text{s}$

References

- [1] Seigman A., *Lasers*, University Science Books, Sausalito, CA, (1986).
- [2] Pound R.V., *Electronic Frequency Stabilization of Microwave Oscillators*, Rev. Sci. Instr. **17**(11): 490-505, (1946).
- [3] Drever R.W.P., Hall J.L., Kowalski F.L., Hough J., Ford G.M., Munley A.J., and Ward H., *Laser Phase and Frequency Stabilization Using an Optical Resonator*, App. Phys. B **31**(2): 97-105, (1983).
- [4] Black E., *An Introduction to Pound-Drever-Hall Laser Frequency Stabilization*, Am. J. Phys **69**(1): 490-505, (2001).
- [5] Bender P.L., Danzmann K. and the LISA Study Team, *Laser interferometer space antenna for the detection of gravitational waves Pre-Phase A Report*, Doc. MPQ 233, (1998).
- [6] Alnis J., Matveev A., Kolachevsky N., Udem Th., and Hänsch T. W., *Subhertz linewidth diode lasers*, Phys. Rev. A, **77**, 053809, (2008).
- [7] Thorpe J.I., Numata K., Livas J., *Laser Frequency Stabilization and Control through offset sideband locking to optical cavities* Opt. Ex. **16**(20):15980-15990, (2008).
- [8] de Vine G. and Shaddock D.A., *Ongoing investigations at the Jet Propulsion Laboratory*, Pasadena, CA, 2008.
- [9] Leonhardt V. and Camp J., *Space interferometry application of laser frequency stabilization with molecular iodine*, App. Opt. **45**, 4142, (2006).
- [10] Bjorklund G.C., *Frequency-modulation spectroscopy: a new method for measuring weak absorptions and dispersions*, Opt. Lett. **5**, 15, (1979).
- [11] Shirley J.H., *Modulation transfer processes in optical heterodyne saturation spectroscopy*, Opt. Lett. **7**, 537, (1982).
- [12] Heinzel G., Braxmaier C., Schilling R., Rudiger A., Robertson D., te Plate M., Wand V., Arai K., Johann U., and Danzmann K., *“Interferometry for the LISA technology package (LTP) aboard SMART-2”*, Class. Quantum Grav. **20**, S153–S161 (2003).
- [13] Heinzel G., Wand V., Garcia A., Jennrich O., Braxmaier C., Robertson D., Middleton K., Hoyland D., Rudiger A., Schilling R., Johann U., and Danzmann K., *“The LTP interferometer and phasemeter”*, Class. Quantum Grav. **21**, S581–S587 (2004).
- [14] Sheard B.S., Gray M.B., McClelland D.E., and Shaddock D.A., *Physics Letters A* **320**, **9** (2003).

- [15] Marin A.F.G., Heinzel G., Schilling R., Wand V., Cervantes F.G., Steier F., Jennrich O., Weidner A., and Danzmann K., *Class. Quantum Grav.* **22**, p. S235. (2005)
- [16] Thorpe J.I. and Mueller G., *Physics Letters A* **342** 199-204 (2005)
- [17] Sheard B.S., Gray M.B., and McClelland D.E., *Applied Optics*, **45** 8491-8499 (2006).
- [18] Wand V., Yu Y., Mitryk S., Sweeney D., Preston A., Tanner D., Mueller G., Thorpe J.I., and Livas J., *J. of Phys: Conference Series*, **154** 012024, (2009).
- [19] Sylvestre J., *Phys. Rev. D* **70**, 102002 (2004).
- [20] Tinto M., Rakhmanov M., *On the laser frequency stabilization by locking to a LISA arm*, arXiv:gr-qc/0408076v1 (2004).
- [21] Sutton A., and Shaddock D.A., *Phys. Rev. D* **78**, 082001, (2008).
- [22] Herz M., *Opt. Eng. (Bellingham, Wash.)*, **44**, 090505, (2005).
- [23] Tinto M., Shaddock D.A., Sylvestre J., and Armstrong J.W., *Phys. Rev. D* **67** (2003).
- [24] Heinzel G., Braxmaier C., Danzmann K., Gath P., Hough J., Jennrich O., Johann U., Rudiger A., Sallusti M., and Schulte H., *Classical and Quantum Gravity*, **23**, S119-S124 (2006)
- [25] Tinto M., Estabrook F.B., and Armstrong J.W., *Phys. Rev. D* **65**, 082003 (2002).
- [26] Tinto M., Estabrook F.B., and Armstrong J.W., *Phys. Rev. D* **69**, 082001 (2004).
- [27] Hellings R.W., Giampieri G., Maleki L., Tinto M., Danzmann K., Hough J., and Robertson D., *Optics Comm.* **124** 313-320 (1996).
- [28] Hellings R.W., *Phys. Rev. D* **64** 022002 (2001)
- [29] de Vine G., Shaddock D.A., Spero R.E., Ware B., McKenzie K., and Klipstein W., in preparation (2009)
- [30] McKenzie K., Spero R.E., and Shaddock D.A., *The performance of arm locking in LISA*, Submitted to *Phys. Rev. D*
- [31] Gath P., Arm Locking Configurations, LISA performance engineering technical note, LPE-ASD-TN-0005 (2009).
- [32] Gath P., Payload Control Systems, LISA mission formulation technical note, LISA-ASD-TN-2004 (2006).
- [33] Tinto M. and Armstrong J.W., *Cancellation of laser noise in an unequal-arm interferometer detector of gravitational radiation* *Phys. Rev. D* **59**, 102003, (1999).

- [34] McKenzie K. and Shaddock D.A., *TDI Capabilities and Frequency Noise Requirements*, LISA Tech. Note LIMAS-2008-001 (2008).
- [35] LI-AEI-TN-3013b AEI Technical Note in preparation.
- [36] Shaddock D.A., Ware B., Halverson P., Spero R.E., Klipstein W., *Overview of the LISA Phasemeter* AIP Conf Proc. **873** 654-60, (2006).
- [37] Misra P. and Enge P. (2nd Ed) *Global positioning system, signals, measurements, and performance*, Ganga-Jamuna Press, (2001).
- [38] Cornish N.J. and Hellings R.W., *Class. Quantum Grav.* **20**, p 4851-4860 (2003)
- [39] Shaddock D.A., Ware B., Spero R.E., and Vallisneri M., *Postprocessed time-delay interferometry for LISA*, *Phys Rev D*, **70**, 081101, (2004).
- [40] Shaddock D.A. and Ware B. Data rates and interpolation error, JPL Technical Note LIMAS 2005-001 (2005)
- [41] Spero R.E., et al *Range measurement for LISA* 8th Edoardo Amaldi Conference, Columbia University June (2009)
- [42] Robertson D. and Ward H. *Scattered Light*, Technical Note L2-UGL-TN-3001 Version 1.0 January, (2009).